



# Flight mechanical analysis of a solar-powered high-altitude platform

Yasim J. Hasan<sup>1</sup> · Mathias S. Roeser<sup>1</sup> · Martin Hepperle<sup>2</sup> · Steffen Niemann<sup>3</sup> · Arne Voß<sup>4</sup> · Vega Handjo<sup>4</sup> · Christian Weiser<sup>5</sup>

Received: 28 March 2022 / Revised: 30 August 2022 / Accepted: 18 October 2022 / Published online: 7 November 2022  
© The Author(s) 2022

## Abstract

The German Aerospace Center (DLR) is currently developing an unmanned experimental solar-powered fixed-wing high-altitude platform designed to be stationed in the stratosphere for several days and to carry payload for earth observation missions. This paper deals with a flight mechanical analysis of the aircraft within the preliminary design phase. For this purpose, it briefly describes all disciplines involved in the preliminary design and gives an insight into their methods used. Subsequently, it presents an assessment of the aircraft in terms of stability and control characteristics. Doing so, it first deals with a dynamic stability investigation using a non-linear 6-degrees-of-freedom flight dynamic model with a simple quasi-stationary approach to account for flexibility, in which the aerodynamic derivatives are given for different airspeed-dependent flight shapes. The investigations show that the aircraft is naturally stable over the complete flight envelope. It does not have a typical short period mode. Instead, the corresponding mode involves altitude and airspeed changes to a large extent. At low airspeeds, the Dutch roll and spiral modes couple and form two non-classical modes. Second, it presents a control surface design evaluation process for the aircraft based on a flight mechanical requirement. This requirement addresses the necessary control authority to counteract the aircraft's responses due to gust encounters to not exceed afore-defined limits and to prevent the aircraft from entering a flight condition that it cannot be recovered from.

**Keywords** High-altitude platform · Solar-powered aircraft · Flight mechanics · Preliminary design · Gust encounter simulations · Stability and control

## Abbreviations

6DOF	Six-degrees-of-freedom	EASA	European union aviation safety agency
AVL	Athena vortex lattice	ERAST	Environmental research aircraft and sensor technology
CS	Certification specifications	FDM	Flight dynamic model
DLR	Deutsches Zentrum für Luft und Raumfahrt (German Aerospace Center)	FL	Flight level (e.g., FL 100 $\hat{=}$ 10,000 ft)
		HALE	High-altitude long-endurance
		HAP	High-altitude platform
		HAPs	High-altitude platforms
		HTP	Horizontal tailplane
		JARUS	Joint authorities of rulemaking on unmanned systems
		MIT	Massachusetts institute of technology
		NASA	National aeronautics and space administration
		SAR	Synthetic aperture radar
		SORA	Specific operational risk assessment
		TLAR	Top-level aircraft requirements
		VLM	Vortex lattice method
		VTP	Vertical tailplane

✉ Yasim J. Hasan  
yasim.hasan@dlr.de

<sup>1</sup> Institute of Flight Systems, German Aerospace Center (DLR), Lilienthalplatz 7, 38108 Braunschweig, Germany

<sup>2</sup> Institute of Aerodynamics and Flow Technology, German Aerospace Center (DLR), Lilienthalplatz 7, 38108 Braunschweig, Germany

<sup>3</sup> Institute of Composite Structures and Adaptive Systems, German Aerospace Center (DLR), Lilienthalplatz 7, 38108 Braunschweig, Germany

<sup>4</sup> Institute of Aeroelasticity, German Aerospace Center (DLR), Bunsenstr. 10, 37073 Göttingen, Germany

<sup>5</sup> Institute of System Dynamics and Control, German Aerospace Center (DLR), Münchener Straße 20, 82234 Weßling, Germany

**List of Symbols**

$b$	Span
$\bar{c}$	Mean aerodynamic chord
$C_l, C_m, C_n$	Body-axes moment coefficients
$C_L, C_D$	Lift and drag coefficients
$C_X, C_Y, C_Z$	Body-axes force coefficients
$C_{x_1, x_2}$	Derivative of $x_1$ due to $x_2$
$D$	Damping ratio
$e$	Oswald efficiency factor
$e_\theta$	Pitch attitude error
$g$	Acceleration due to gravity
$H$	Altitude
$i_{HTP}$	Horizontal tailplane deflection
$I_x, I_y, I_z, I_{xz}$	Mass moments of inertia
$k_{HTP, eff}$	Horizontal tailplane effectiveness factor
$k_{\xi, eff}$	Aileron effectiveness factor
$k_{\zeta, eff}$	Rudder effectiveness factor
$K$	Flight controller gains
$m$	Mass
$n_y$	Body-fixed lateral load factor
$p, q, r$	Body-fixed rotational rates
$p^*, q^*, r^*$	Non-dimensional body-fixed rotational rates
$\bar{q}$	Dynamic pressure
$s$	Semispan
$S$	Reference area
$t$	Time
$T$	Engine thrust
$u_K, v_K, w_K$	Inertial translational velocities
$u_W, v_W, w_W$	Wind component velocities
$V_{EAS}$	Equivalent airspeed
$V_{NE}$	Never-exceed speed
$V_{O, max}$	Maximum operating speed
$V_{O, min}$	Minimum operating speed
$V_S$	Stalling speed
$V_{TAS}$	True airspeed
$x_{HTP}$	Longitudinal distance between horizontal tailplane neutral point and wing-body neutral point
$x'_{HTP}, z'_{HTP}$	Longitudinal and vertical distances between horizontal tailplane neutral point and centre of gravity
$x'_{WB}, z'_{WB}$	Longitudinal and vertical distances between wing-body neutral point and centre of gravity
$x, y, z$	Positions
$\hat{y}$	Measured state vector
$\alpha$	Angle of attack
$\beta$	Angle of sideslip
$\gamma$	Flight path angle
$\partial\epsilon/\partial\alpha$	Downwash angle change due to change of angle of attack
$\epsilon$	Downwash angle
$\epsilon_{0HTP}$	Downwash angle at HTP for $\alpha = 0^\circ$
$\Lambda$	Aspect ratio ( $\Lambda = b^2/S$ )

$\Phi, \Theta, \Psi$	Euler angles
$\rho$	Air density
$\tau$	Time delay
$\xi_l, \xi_r$	Left/right aileron deflection
$\xi$	Combined left and right aileron deflection
$\zeta$	Rudder deflection

**Indices**

0	Initial, reference or sea level value
A	Air path value
b	Body-axis coordinate system
cmd	Commanded
dyn	Dynamic
dr	Dutch roll
K	Flight path value
max	Maximum value
meas	Measured value
min	Minimum value
ph	Phugoid
r	Roll
ref	Reference value
s	Spiral
sp	Short period
W	Wind value
WB	Wing-body

**1 Introduction**

A high-altitude platform (HAP, *pl.* HAPs), sometimes also referred to as high-altitude long-endurance (HALE) aircraft, is an air vehicle operating at high altitudes and usually for a prolonged time span. Unmanned solar-powered HAPs can, in theory, even be operated permanently or, in practice, at least for several weeks before landing becomes necessary again [1]. Flying in the lower stratosphere, HAPs are located above commercial air traffic and thus do not interfere with most passenger aircraft. In recent years, research work on HAPs has increased intensely and several projects about HAPs of different air vehicle type have been launched [2].

HAPs bring benefits with respect to several use cases. While they can be operated continuously for a much longer time span than conventional air vehicles, their trajectories can mostly be freely chosen in contrast to satellites whose positions along with the associated passing times are dependent on their orbit. Thus, combining the advantages of satellites with those of air vehicles, HAPs represent excellent candidates for general earth observation missions [3], surveillance in case of humanitarian crises or natural catastrophes, support for agricultural tasks or health monitoring for, as an example dykes. Furthermore, the lower altitude compared to satellites allows for higher resolution observation images and no space debris is left

after the HAP's decommissioning. Other use cases include telecommunications. Thanks to the flexible usability, HAPs can be used to provide internet and radio network both to areas with bad telecommunications infrastructure, e.g., conflict areas or regions where natural disasters have occurred, and to places where additional bandwidth is needed transitionally, for instance due to events like music festivals. Moreover, a HAP's higher altitude allows for a better coverage compared to usual radio masts while enabling much shorter signal paths than satellites. Hence, the introduction of an additional HAP-based telecommunications system supporting and connecting the terrestrial and satellite-based systems seems highly beneficial [4].

The progress in structural design and ultralight construction, battery technology and solar devices has forwarded the research and development of HAPs since the late 90s. Some of the most prominent HAP-related programmes are the NASA ERAST programme [5] producing a great number of aircraft, including the Helios aircraft which holds the current altitude record among HAPs of 96,863 feet [6], the Solar Impulse programme [7], which realised a fully solar-powered manned flight around the world, covering a distance of around 26,718 miles in 2016 [8] and the Airbus Zephyr programme [9] featuring the Zephyr S which recently broke its own endurance record among HAPs of nearly 26 days in 2018 [1] by a 64-day continuous flight performed from June to August 2022 [10].

However, the design and operation of HAPs are a challenging task, as a broad number of mishaps prove [11–14]. For fixed-wing aircraft, the goal of high endurance requires a very low weight and a very high aspect ratio for realising high aerodynamic efficiency. At the same time, the necessary batteries to store enough energy for maintaining a minimum altitude over night brings a considerable weight penalty. A harmonisation of these factors imposes an ultralight structure which leads to a very flexible aircraft. Another issue is the very large flight envelope with respect to altitude ranging from sea level to the lower stratosphere in combination with the absence of a high-lift system due to aircraft weight restrictions. As a consequence, the allowable speed range is very small. As the aircraft operates unmanned and beyond the line of sight, it needs to be equipped with a termination system, which brings another weight penalty. In order to not have to terminate the aircraft immediately if the communication between ground segment and aircraft is interrupted for a couple of seconds and in order to save control energy, the design of a naturally stable aircraft is advantageous. In sum, the development of a HAP needs thorough flight mechanical investigation, analysis and sizing.

In the context of the project *High-Altitude Platform (HAP)*, the German Aerospace Center (DLR) develops a HAP system designated to perform earth observation

missions carrying a payload of up to 5 kilogrammes. For these missions either a high-definition camera or a synthetic aperture radar (SAR) is to be used. It was decided a priori that the underlying vehicle should be a fixed-wing aircraft that dynamically generates lift rather than an airship. First, this choice is based on the need for station-keeping for the missions. Due to performance reasons, airships typically have a lower airspeed, wherefore at higher wind speeds, their ability to stay above a certain point over ground is limited. Second, for a payload of 5 kg, the required airship size would be significantly higher than for an aircraft [15]. The HAP system includes the aircraft itself, the flight control system and the full operational concept, the ground segment, the flight termination system and the two use case instruments. The development of the HAP aircraft contains the conceptual, preliminary and detail design phases, the aircraft fabrication, a flight test campaign and final high-altitude mission demonstrations using the use case instruments. Flight permissions are planned to be obtained based on the specific operational risk assessment (SORA) [16] developed by the Joint Authorities of Rulemaking on Unmanned Systems (JARUS) and endorsed by the European Union Aviation Safety Agency (EASA) [17].

In the last decades, DLR has been involved in the development of multiple HAP, respectively HALE aircraft in the context of several projects [18]. However, since these works, the technology of the underlying systems and particularly the research on such aircraft progressed largely. Therefore, these works did not form a basis for the current HAP design. Instead, the aircraft was developed from scratch starting with conceptual analyses. Nevertheless, some of the experience and knowledge obtained within the prior projects proved to be helpful in designing the current HAP aircraft.

There are already a great number of current programmes worldwide that focus on the design and operation of HAP aircraft. The Airbus Zephyr [9], the BAE Systems PHASA-35 [19] or the UAVOS ApusDuo [20] are only some prominent examples of aircraft that also already performed successful flights. However, current programmes are usually part of commercial projects, whose primary aim is to create business or military use cases. To the best of the authors' knowledge, no publications are available that focus on detailed scientific results and analyses of HAP aircraft. Therefore, the primary aim of the DLR project *HAP* is to obtain, generate and publish knowledge about such aircraft rather than to compete with the HAP aircraft developed by industrial companies.

This paper focusses on the analyses of the HAP aircraft's flight mechanics in the preliminary design phase. For this purpose, Sect. 2 briefly describes the steps performed to find an initial aircraft design, outlines the preliminary design process and presents the disciplinary methods and models used in the fields of aerodynamics, structures,

aeroelastics, flight dynamics and flight control to obtain the flight dynamic model of the aircraft. Section 3 deals with the flight mechanical analysis of the HAP. It starts with an investigation of the aircraft's eigenmodes in the complete flight envelope. In addition, this paper proposes an approach on how to assess the need for control surface authority based on gust encounter simulations using a flight control system and applies it for the DLR HAP aircraft. Based on a defined requirement, the simulated aircraft reactions as well as its gust rejection capabilities are used to evaluate the control surface design. Finally, Sects. 4 and 5 close this paper with a conclusion and a brief outline of the future work.

The HAP aircraft dealt with in this paper represents the current configuration within the preliminary design phase. It will, therefore, be subject to further design changes as the project progresses and the design becomes more detailed. Nevertheless, the authors believe that the proposed configuration is feasible from an overall point of view and only minor design changes are expected. The results and the design decision methodology presented in this paper are representative.

## 2 Design of the DLR HAP aircraft

This section presents the steps performed to develop the DLR HAP aircraft. It briefly presents the different disciplines involved in the preliminary design phase and shows the general interplay between the different disciplines. Furthermore, it describes some of the disciplinary methods and lists the assumptions and results that are fundamental for the flight mechanical analyses presented in Sect. 3.

### 2.1 Initial aircraft configuration

First of all, an initial HAP configuration in terms of high-level parameters like wing area, wing span, masses, etc. needs to be found, which is promising with respect to fulfilling all top level aircraft requirements (TLAR). The TLAR also include a specification that requires the HAP to be operated for at least 30 days at certain geographical earth coordinates carrying a payload of 5 kilogrammes and within respective time spans before landing again. Thus, besides using typical conceptual design methods to dimension the aircraft, a high-level mission simulation that takes into account the overall energy balance of the aircraft is performed. Based on the TLAR, user inputs like wing loading, wing span etc., geographic latitude and a starting time of the year, horizontal tailplane (HTP) and vertical tailplane (VTP) are sized, aerodynamic lift and drag is calculated and masses are approximated. The difference

between the resulting aircraft mass and a target mass of 140 kg is fully used to include batteries.

The aircraft is then regarded as a point mass and a simple kinematic mission is performed using a simulation step time of 15 minutes. The HAP performs a single flight consisting of a go-and-return track. At the same time, energy due to solar radiation is stored in the batteries respecting the local incidence angle at the respective solar cells and the degree of solar cell coverage on the wing. Having reached a predefined battery state of charge, a simple controller commands the aircraft to gain altitude using excess solar power. During night, altitude is first reduced until the minimum altitude is reached. Subsequently, the energy out of the battery is used to maintain the minimum altitude until solar energy is again available after sun dawn. During the times of the day when there is not much solar radiation available, particularly at dawn and before sunset, the HAP's heading is adjusted in such a way that solar energy gain is maximised. The battery state of charge is monitored. If it has never fallen below 20 % during the complete mission simulation, the configuration (defined by wing area, wing span, tailplane size and battery mass) is classified as feasible.

Figure 1 shows an exemplary mission profile for a configuration candidate. Part 1a shows the altitude pattern and part 1b depicts the battery state of charge over the complete simulation time.

### 2.2 Preliminary design

In the context of the preliminary design phase, this initial HAP configuration is analysed and designed in more detail. Figure 2 shows a sketch of the interplay of all disciplines involved in the preliminary design of the DLR HAP aircraft, the main dependencies and the exchange of the most relevant

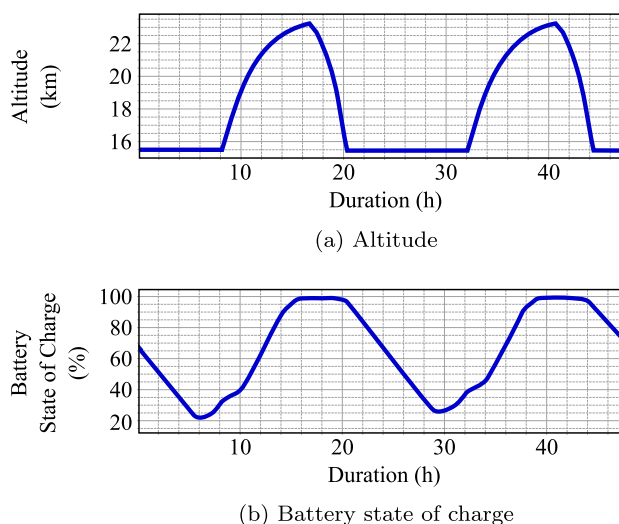
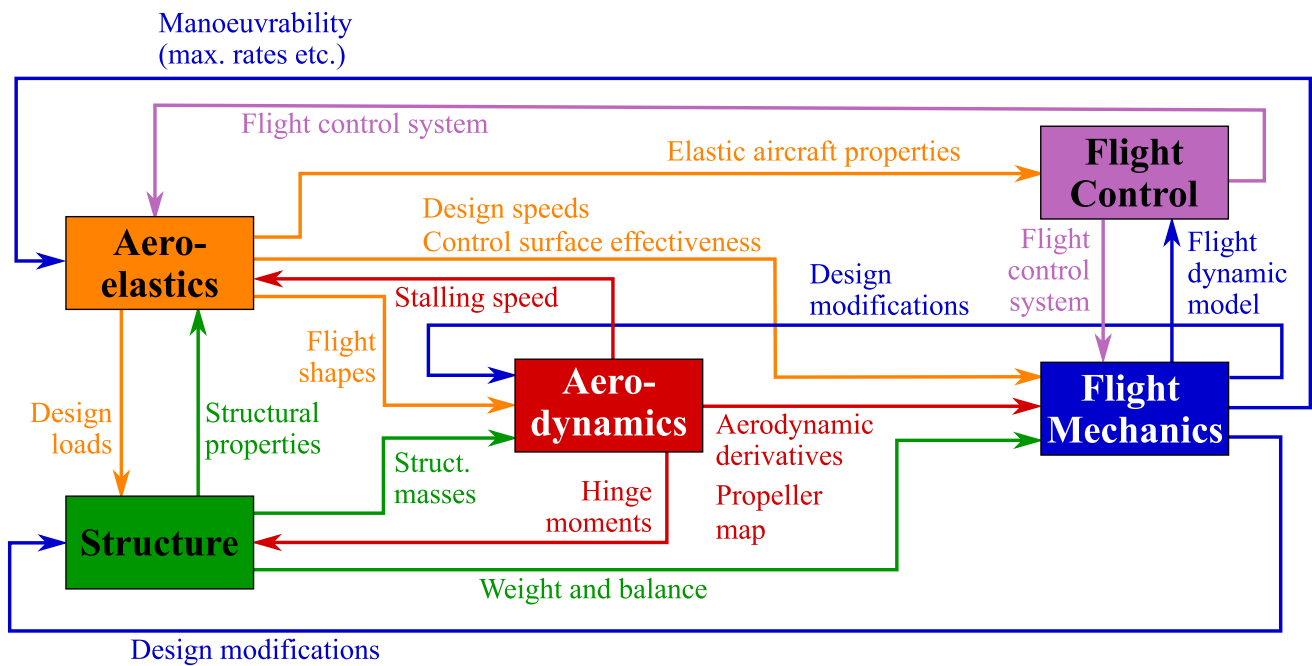


Fig. 1 Exemplary mission profile



**Fig. 2** Sketch of the preliminary design working group, the disciplinary interplay and the exchange of aircraft data and results

aircraft data and results. Note that Fig. 2 does not present a general design methodology.

As shown, the fields of aerodynamics, structure, aeroelastics, flight mechanics and flight control are involved and strongly interdependent. As will be explained in detail in Sect. 3, control surface geometry choice will be mainly driven by gust rejection simulations using control surfaces. Therefore, a flight control system needs to be used and its implementation process is thus part of the preliminary design framework.

The design of a HAP aircraft is, due to its challenging TLAR, particularly driven by compromises between all disciplines. Therefore, the disciplinary tasks require thorough consideration and more detailed analyses than performed with typical preliminary design chains used for more conventional aircraft.

The complete design process consists of a consecutive series of design loops. For instance, a modification of the VTP leads to the necessity of a resizing of the structural masses, which imposes the need of re-calculating the design loads. Aerodynamic derivatives change and, as a consequence, the flight dynamic model needs to be updated. After adjusting the flight control system, the aircraft can be assessed again.

In the following, all involved disciplines are presented in more detail.

### 2.2.1 Aerodynamic design and analysis

The aerodynamics of a HAP aircraft are characterised by the low wing loading and hence low flight speeds. The combination with the geometry and the wide range of operating altitudes requires relatively high-lift coefficients at low Reynolds numbers. The Reynolds number covers a range from man carrying sailplanes down to radio-controlled model aircraft. These low Reynolds numbers together with the desired lift coefficients in the order of 1.5 drive wing and airfoil design. Airfoil thickness and camber are limited due to Reynolds number and structural constraints.

Due to the unswept, high aspect ratio wing planform, classical methods based on potential theory are well suited for this task. In this case, the classical vortex lattice method (VLM) *Athena Vortex Lattice* (AVL), developed at MIT [21, 22] was used. Besides the basic VLM this tool also offers very useful modules for trim and preliminary stability and control calculations.

First, AVL was used to determine a suitable twist distribution of the wing to achieve low induced drag and safe stall characteristics. The spanwise lift distributions at different flight speeds then served as requirements for the airfoil design.

Airfoils were designed with inverse design tools [23–25] taking the given ranges of lift coefficient and Reynolds number into account. Within the typical operating range of the DLR HAP, the airfoil sections of the main wing produce lift coefficients between 0.6 and 0.9, extending up to 1.6

at high-altitude stall speed and down to 0.2 at dive speed. The Reynolds number covers a range from man carrying sailplanes down to radio-controlled model aircraft. At 25 km altitude, the airfoils operate at Reynolds numbers less than 200,000 while at the maximum operating speed at sea level they are operated at around 1,500,000. The airfoil design tried to minimise concave surfaces to simplify covering the wing with heat-shrink film. Furthermore, the pitching moment coefficient was constrained to limit torsional loads at higher flight speeds. To simplify the manufacturing process, only two airfoils were designed: one for the rectangular inboard wing and one with reduced camber for the transition to the wing tip. In all cases, turbulent flow on the upper surface due to the integration of the solar cells was assumed.

The aerodynamic design of the wing tried to combine low induced drag with the heavy structural constraints. Especially the torsion moment strongly affected the design of the tip airfoil and its reduced pitching moment resulted in weight savings in the inboard wing spar. To obtain a soft stall, the spanwise lift distributions at higher angles of attack were analysed and the design of the airfoil sections adapted so that wing stall should occur first on the inboard wing, minimising the risk of a stall induced roll or spin.

In the first design phase, no complete structure and mass model existed for generating the aerodynamic database. Nevertheless, it was desired to consider effects of flexibility over the range of design speeds. For this purpose, the flight shape of the rigid wing was bent and twisted according to the results of the preliminary aeroelastic analysis. Four different shapes were generated for the four design speeds, that will be presented in Sect. 3.1 and for each shape a set of aerodynamic derivatives was calculated using AVL.

For this work, a mesh transformation module, which had already been integrated into AVL, was used. This module transforms all vortex lattice grid points according to prescribed transformation schemes (shearing, rotating, bending, twisting) before the numerical analysis is performed. Thus, the same rigid input geometry can be used and is transformed to the desired shape for each flight speed.

The results comprise static and dynamic derivatives as well as control surface derivatives for the deformed, but rigid aircraft at four flight speeds. Similarly, derivatives for ground proximity were generated. It is clear that this approach represents only a rough static model of a quasi-flexible aircraft, but this was considered to be acceptable for deriving a flyable configuration during the first design phase. Additional effects of flexibility were added later, such as a reduction of control surface efficiency. A fully flexible model of the aircraft is currently under development as described in Sect. 2.2.3.

Finally, limits for a stall model were derived from the development of the spanwise lift distribution when approaching stalling speed  $V_S$ .

Besides the aerodynamic design of the vehicle, some effort was spent into the design of the propellers for the HAP aircraft. These must produce almost the same thrust over the altitude envelope, but with low power and rpm at low altitude and with high power and rpm at high altitude. The design was performed with an inverse design method based on the classical theory of minimum loss propellers [26–29] implemented in the blade element method tool PROPPY [30, 31], similar to the implementation in JavaProp [32]. This tool includes an inverse design module which generates the blade geometry for a propeller of minimum induced losses. Besides a small set of requirements (diameter flight speed, operating altitude and available shaft power and rotational speed) radial distribution of airfoil sections and lift coefficients are prescribed. The resulting geometry can then be analysed in off-design conditions or tweaked by changing twist or chord length distributions. Additional limitations like a torque limit of the electric motor were imposed when the performance of the propeller and the aircraft was evaluated later. This limitation is important for climb performance at low altitude where the propeller rpm is low (from ground to altitude the speed of the propeller varies considerably between 600 and 2000 1/min). Initial design studies with diameter and rotational speed were leading to the final propeller design as a compromise between propeller efficiency and motor mass. PROPPY was also used for the analysis of mission points, windmilling drag and power as well as for determining structural loads. The impact of the very low Reynolds numbers was taken into account by the application of adapted airfoil polars for the propeller blades.

The aerodynamic database for the fixed-pitch propeller consists of a set of characteristics in form of power and thrust coefficient vs. advance ratio.

### 2.2.2 Structure

The preliminary structural sizing process aims to determine the masses, stiffnesses and moments of inertia of the primary airframe structural elements for the HAP aircraft. To achieve a low calculation time at this design level, the sizing is carried out with an algorithm based on analytical methods.

For this purpose, a beam model of the aircraft with all components, namely wing segments, longerons (fuselage, pylons) and tail segments, is generated. For discretisation, all wing and tail ribs as well as frame positions of the longerons define control points where section loads are calculated and exchanged with the aeroelastic load cases.

The mass calculation is performed by dimensioning the main structural elements according to Bernoulli beam theory, namely the wing and tail spars and the longeron-like

fuselage and engine nacelles. The masses of other elements like ribs, wing fairings including solar generators or joining elements are scaled volumetrically or two-dimensionally.

A tubular beam is chosen as the main structural element of the wing spars and as longerons. There are multiple reasons for this choice. First, the very low wing loading results in a very thin laminate thickness. Second, manufacturing aspects, e.g. winding technology vs. costs for shell tools or assembly considerations play a role.

The sizing criteria of the beam elements are material strength [33], stability [34] and demands on torsional and bending stiffness. The dimensioning parameters are the tube thickness, tube diameter, the rib or frame distance and material parameters (laminate stacking). As material model, a smeared winding laminate is considered, such that the thickness is the only design parameter, while different laminates with different smeared stiffness and strength properties are selectable. A minimum material thickness prevents non-producible wall thicknesses.

The design process between load calculation and structural sizing is realised iteratively, starting with an initial structural design, followed by several load and sizing loops.

### 2.2.3 Aeroelasticity

The aeroelastic modelling of the structure, visualised in Fig. 3, uses a finite elements model with beam elements, which represent the long and slender structure adequately and are very close to the actual structural design. The beam model is discretised at every rib station along the wing and comprises a leading and trailing edge connected with rigid body links to the main spar. The main purpose is to investigate effects such as the wing torsion. Structural masses are derived from the thickness and density of the

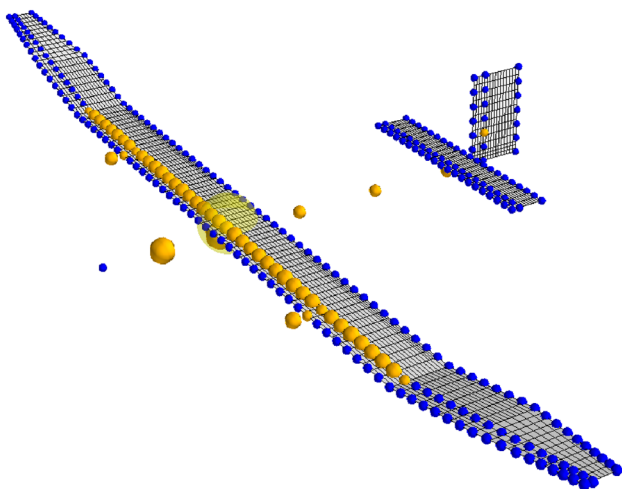


**Fig. 3** Structural discretisation (blue), condensed masses (yellow) and aerodynamic panel mesh of the aeroelastic model

material. The non-structural masses of the wing include the solar generators, the battery packs and the engines. Since the torsional eigenmodes and eigenfrequencies of the wing are very sensitive, special attention needs to be put on the inertia properties about the  $y$ -axis and the location of the masses in  $x$ -direction. Both mass and inertia properties are then modelled as condensed masses, which are attached to the structural grid points of the finite elements model.

The flight speed is fully within the subsonic regime and panel methods such as the steady VLM using horseshoe vortices yield an acceptable representation of the lifting surfaces. In a next step, the impact of the aerodynamic forces on the structure needs to be evaluated. Formally, the coupling can be handled using a transformation matrix which relates displacements of the structural grid to displacements of the aerodynamic grid. The forces and moments are transferred from the aerodynamic grid to the structural grid. More details on the aeroelastic model are given in [35]. With this basis, a number of aeroelastic analyses are conducted, described briefly in the following.

In a first step, a comprehensive loads analysis is performed, including manoeuvre loads, dynamic gust loads, landing loads and gyroscopic loads. The resulting section loads are used for the structural sizing. A heavier and/or stiffer structure results in a change in loads, which leads to an iterative process of loads analysis and structural sizing. After convergence is established, the desired flight shape is defined by the aerodynamic specialists for best performance in cruise flight conditions. In this regard, the wing twist is of principal interest with respect to a favourable lift distribution while the wing bending is negligible. Due to the elastic deformations, the jig shape needs to be adapted in such a way that the flight shape is matched. Also, the wing flexibility needs to be considered for lateral stability analyses as the elastic wing bending adds to the geometrical dihedral. The elastic behaviour of the empennage and the fuselage leads to a shift of the aerodynamic centre, which influences the longitudinal stability. Finally, the aeroelastic control surface effectiveness is evaluated, which is important for controllability and manoeuvrability.

The calculations are performed at selected operational conditions using MSC.Nastran SOL144 [36, 37] and the LoadsKernel [38] software. The data are then provided for use in flight mechanical analyses in a tabular form and intermediate values are interpolated. For the fully flexible flight mechanical model mentioned in Sect. 2.2.4, aerodynamic derivatives with respect to the elastic modes will be added to the dataset.

### 2.2.4 Flight dynamic model

For the flight dynamic analysis within the *HAP* project an aircraft simulation model is used. The aircraft is described

by a classical non-linear six-degrees-of-freedom (6DOF) dynamic model. The model description below is mainly the same as also used for highly accurate simulator models meeting Level-D simulator certification criteria [39, 40].

The translational motion for a thrust vector  $T$  which is aligned with the body axis is given by

$$\begin{aligned} \dot{u}_K &= r v_K - q w_K + \frac{\bar{q}S}{m} C_X - g \sin \Theta + \frac{T}{m} \\ \dot{v}_K &= p w_K - r u_K + \frac{\bar{q}S}{m} C_Y + g \cos \Theta \sin \Phi \\ \dot{w}_K &= q u_K - p v_K + \frac{\bar{q}S}{m} C_Z + g \cos \Theta \cos \Phi, \end{aligned} \tag{1}$$

where the flight path velocity components are a sum of the air path velocity components and the wind:

$$\begin{bmatrix} u_K \\ v_K \\ w_K \end{bmatrix} = \begin{bmatrix} u_A \\ v_A \\ w_A \end{bmatrix} + \begin{bmatrix} u_W \\ v_W \\ w_W \end{bmatrix}. \tag{2}$$

The rotational motion for a symmetric aircraft about the  $xz$ -plane and, for the sake of simplicity given here for symmetric thrust aligned with the body axis, is described as

$$\begin{aligned} \dot{p} I_x - \dot{r} I_{xz} &= \bar{q} S s C_l - q r (I_z - I_y) + p q I_{xz} \\ \dot{q} I_y &= \bar{q} S \bar{c} C_m - p r (I_x - I_z) - (p^2 - r^2) I_{xz} \\ \dot{r} I_z - \dot{p} I_{xz} &= \bar{q} S s C_n - p q (I_y - I_x) - q r I_{xz}. \end{aligned} \tag{3}$$

The longitudinal motion aerodynamics are based on a two-point model, allowing a separate consideration of main wing and HTP aerodynamics, as described in [41, 42]. This model enables to account both for a lag effect of the wing downwash and for different passing times of oncoming longitudinal and vertical wind components at the HTP. This is particularly important for the modelling of a HAP aircraft since due to the aircraft’s low airspeed, the time lag is, with values up to nearly 1 second, relatively high. Herein, the lift coefficient is separated into a wing-body (WB) component and a component for the horizontal tail (HTP). These are calculated as

$$\begin{aligned} C_{L_{WB}} &= C_{L0_{WB}} + C_{L\alpha_{WB}} \alpha + C_{Lq_{WB}} q^*, \\ C_{L_{HTP}} &= C_{L0_{HTP}} + C_{L\alpha_{HTP}} \alpha_{HTP} k_{HTP,eff}, \end{aligned} \tag{4}$$

with the nondimensional pitch rate

$$q^* = \frac{q \bar{c}}{V_{TAS}}. \tag{5}$$

The resulting lift coefficient is given by

$$C_L = C_{L_{WB}} + C_{L_{HTP}} \frac{S_{HTP}}{S} \cos(\alpha_{dyn} - \epsilon_{HTP} + \Delta\alpha_{W_{HTP}}), \tag{6}$$

where  $\Delta\alpha_{W_{HTP}}$  is the difference of the angles of attack due to wind between the HTP and the wing, calculated as

$$\begin{aligned} \Delta\alpha_{W_{HTP}} &= \alpha_{W_{HTP}} - \alpha_W \\ \alpha_{W_{HTP}} &= \alpha_W(t - \tau). \end{aligned} \tag{7}$$

The term  $\alpha_{W_{HTP}}$  describes the delayed wind component at the HTP,  $\alpha_W$  is the wind component applied to the aircraft wing and  $\tau$  is the time delay until a fluid element reaches the HTP after passing the wing:

$$\tau = \frac{x_{HTP}}{V_{TAS}}. \tag{8}$$

The pitching moment coefficient is also composed of wing-body and HTP components. It is calculated, neglecting the respective drag components, using the body-axis coefficients for wing-body

$$\begin{aligned} C_{X_{WB}} &= C_{L_{WB}} \sin(\alpha), \\ C_{Z_{WB}} &= -C_{L_{WB}} \cos(\alpha), \end{aligned} \tag{9}$$

the body-axis coefficients for the HTP

$$\begin{aligned} C_{X_{HTP}} &= C_{L_{HTP}} \sin(\alpha_{HTP}), \\ C_{Z_{HTP}} &= -C_{L_{HTP}} \cos(\alpha_{HTP}), \end{aligned} \tag{10}$$

and the respective lever-arms:

$$\begin{aligned} C_m &= C_{m0_{WB}} + C_{Z_{WB}} \frac{x'_{WB}}{\bar{c}} - C_{X_{WB}} \frac{z'_{WB}}{\bar{c}} \\ &\quad + C_{Z_{HTP}} \frac{S_{HTP}}{S} \frac{x'_{HTP}}{\bar{c}} - C_{X_{HTP}} \frac{S_{HTP}}{S} \frac{z'_{HTP}}{\bar{c}}. \end{aligned} \tag{11}$$

The angle of attack at the HTP is given by

$$\begin{aligned} \alpha_{HTP} &= \alpha + i_{HTP} + \alpha_{dyn} - \epsilon_{HTP} + \Delta\alpha_{W_{HTP}}, \\ \alpha_{dyn} &= \tan^{-1} \left( q \frac{x'_{HTP}}{V_{TAS}} \right), \\ \epsilon_{HTP} &= \epsilon_{0_{HTP}} + \frac{\partial \epsilon}{\partial \alpha} \alpha(t - \tau). \end{aligned} \tag{12}$$

The downwash angle  $\epsilon_{HTP}$  describes the influence of the wing on the tail, where  $\epsilon_{0_{HTP}}$  is the downwash angle at the horizontal tail for  $\alpha = 0^\circ$ . The control surface effectiveness of the HTP due to flexible deformation as result of a change in angle of attack or stabiliser input is represented in (4) by  $k_{HTP,eff}$ .

The drag coefficient is calculated via the simple polar equation

$$C_D = C_{D0} + \frac{C_L^2}{e\pi\Lambda}. \tag{13}$$



The body-axis force coefficients  $C_X$  and  $C_Z$  from (1) are finally derived from the lift and drag coefficient by

$$\begin{aligned} C_X &= -C_D \cos(\alpha) + C_L \sin(\alpha), \\ C_Z &= -C_D \sin(\alpha) - C_L \cos(\alpha). \end{aligned} \tag{14}$$

The coefficients of the aerodynamic forces and moments for the lateral-directional dynamics ( $C_Y, C_l, C_n$ ) are described by a simple linear approach:

$$\begin{aligned} C_Y &= C_{Y\beta} \beta + C_{Yp} p^* + C_{Yr} r^* + C_{Y\zeta} \zeta \cdot k_{\zeta,eff}, \\ C_l &= C_{l\beta} \beta + C_{lp} p^* + C_{lr} r^* + C_{l\hat{\xi}} \hat{\xi} k_{\xi,eff} + C_{l\zeta} \zeta k_{\zeta,eff}, \\ C_n &= C_{n\beta} \beta + C_{np} p^* + C_{nr} r^* + C_{n\zeta} \zeta k_{\zeta,eff} + C_{n\hat{\xi}} \hat{\xi} k_{\xi,eff}. \end{aligned} \tag{15}$$

Here, the combined aileron deflection  $\hat{\xi}$  is defined as

$$\hat{\xi} = \frac{1}{2}(\xi_r - \xi_l) \tag{16}$$

and the nondimensional roll and yaw rates are

$$\begin{aligned} p^* &= \frac{p s}{V_{TAS}}, \\ r^* &= \frac{r s}{V_{TAS}}, \end{aligned} \tag{17}$$

with the semispan

$$s = \frac{b}{2}. \tag{18}$$

Aileron and rudder effectivenesses due to flexible deformation as result of the control surface deflection are represented in (15) by  $k_{\xi,eff}$  and  $k_{\zeta,eff}$ .

The aerodynamic data for a candidate HAP aircraft configuration are derived from AVL calculations and given in the form of a one-point aerodynamic model. Using an additional value for the HTP lift curve slope from AVL calculations, a separation of the longitudinal aerodynamic derivatives into wing-body and HTP contributions is performed in order to account for the two-point model.

In addition, a stall model as proposed in [43] and a ground effect model as described in [44] are implemented.

The HAP aircraft is a very light and flexible configuration. Its wing deformation is still in the linear elastic regime but during level-flight, the wing tip vertical displacement is around 6% to 7% of the aircraft’s semispan [45]. Although the static deformations of this aircraft are thus not expected to be as huge as e.g. in case of the NASA Helios platform, where the high flexibility led to an accident [11], flexibility needs to be respected to a certain degree in the flight dynamics model. During this stage of the development phase, a quasi-stationary approach with respect to dynamic pressure, respectively equivalent airspeed, is followed. Doing so, a full set of parameters is provided for the

characteristic airspeeds that will be presented in Sect. 3.1. These include the derivatives occurring in Eq. (4) and (15), the zero-coefficients  $C_{L0_{WB}}, C_{L0_{HTP}}$  and  $C_{m0_{WB}}$ , the downwash-related parameters  $\epsilon_{0_{HTP}}$  and  $\partial\epsilon/\partial\alpha$  in Eq. (12) and the control surface effectiveness factors  $k_{\xi,eff}, k_{HTP,eff}$  and  $k_{\zeta,eff}$ . The zero-lift drag coefficient  $C_{D0}$  is additionally given for the specific airspeeds and different altitudes to account for Reynolds number effects. During runtime, interpolation is performed between the aerodynamic derivatives at each time step to account for the airspeed-dependent flight shapes.

At the present design stage, a representation of the flexible mode dynamics as described in [46, 47] is not yet implemented in the flight dynamic model. However, it will be pursued for the further design phases. It will be important to re-evaluate the results presented in this paper respecting the interaction between the flexible dynamics of the structure and the rigid body dynamics.

### 2.2.5 Flight control

For simulation of manoeuvres and especially disturbance rejection scenarios (i.e. gust encounters), the use of a stability and control augmentation system is inevitable in the preliminary design phase of the investigated HAP aircraft. The low wing loading ( $< 5 \text{ kg/m}^2$ ) and low inertia of the HAP lead to a high vulnerability to atmospheric disturbances. Due to the afore-mentioned properties, there is an increased risk that the HAP configuration deviates into stall or over-speed. Therefore, a stability augmentation and attitude control system is designed, which keeps the aircraft within a safe envelope when experiencing external disturbances. With the introduction of this control system in a relatively early design stage, a more realistic approximation of expected structural loads is enabled in addition, which is critical to allow the convergence towards a feasible and realistic aircraft design.

This section gives a brief overview of the used baseline control system which has been developed in [48]. Further development of this attitude control system will allow its use for augmented flight by a remote pilot as well as its employment as an inner loop for the fully automated electronic flight control system.

#### Design requirements

In a first step, stability and performance requirements for the baseline flight control system are derived. These result from design standards, e.g., [49], as well as the expected aircraft and actuator characteristics. The values include classical gain and phase margins for robustness, where the standard 6 dB, respectively,  $45^\circ$  are demanded for low frequencies and increased robustness margins for the frequency region starting from the first structural mode.

When defining the control bandwidth, fast responses are desired with the maximum control bandwidth lower than the

**Table 1** Stability and performance requirements for the baseline flight control system

Name	Value	Frequency
Gain/phase margin	6 dB/45°	[0; 4] rad/s
Gain/phase margin	8 dB/60°	(4; inf) rad/s
Bandwidth	2 rad/s	–
Max. overshoot	< 10%	–

structural mode’s frequencies. This fits well with the time domain goal of rise times of less than 5 seconds which is suggested in [49] for attitude hold functions. An overview of the employed design requirements can be found in Table 1.

**Controller architecture** For the design of the baseline inner loop augmentation, it is common practice to consider longitudinal and lateral-directional axes as sufficiently decoupled to allow separate designs [50]. The architecture of the inner loop control system (Fig. 4) has, therefore, two independent subsystems with pitch angle  $\Theta$  as a reference signal for the longitudinal axis and roll angle  $\Phi$  for the lateral axis. For turn coordination, the lateral acceleration  $n_y$  is used.

For control law synthesis, a 6DOF flight dynamic model is used, which is then truncated into longitudinal and lateral axis sub-models. The vector  $\hat{y}$  in Fig. 4 denotes the measured state vector of the aircraft. This attitude control inner loop design has proven as an intuitive manner of control for unmanned aerial vehicles [51] and has already been implemented and tested in simulations for HAP [48].

**Design of inner loops**

The design of the longitudinal and lateral inner loops depicted in Fig. 4 follows a classical PID control scheme, which has been used for other high aspect ratio flexible aircraft concepts [51].

As an example, the longitudinal inner loop uses the pitch angle  $\Theta$  as a reference signal and the PID control law can be formulated according to

$$i_{HTP} = K_p(\pi) \cdot e_\Theta + K_I(\pi) \cdot e_\Theta + K_D(\pi) \cdot \dot{\Theta}_{meas}, \tag{19}$$

where  $K_p(\pi)$ ,  $K_I(\pi)$  and  $K_D(\pi)$  are the controller gains depending on the scheduling parameter vector  $\pi$ . In case of HAP, the parameter vector consists of equivalent airspeed and altitude, thus  $\pi = [V, h]$ . The pitch attitude error  $e_\Theta$  is defined as

$$e_\Theta = \Theta_{ref} - \Theta_{meas}, \tag{20}$$

where  $\Theta_{ref}$  is the commanded reference attitude. A similar control structure is chosen for the lateral inner loop, which can be found in [48].

**Design technique**

The gains  $K$  of the fixed-structure control architecture described above are tuned within a constrained optimisation process as, e.g. proposed in [52]:

$$\begin{aligned} &\min_{K(\pi)} \left( \max_{i,k} \left( f_i^{(k)}(K(\pi)) \right) \right) \\ &\text{subject to } \max_{j,k} \left( g_j^{(k)}(K(\pi)) \right) < 1 \\ &K_{\min} < K(\pi) < K_{\max} \end{aligned} \tag{21}$$

The optimisation employs the aircraft model presented within this work, which is linearised on a grid of steady-state operating points in the flight envelope. The model includes simplified actuator and sensor dynamics.

The used optimisation constraints  $g$  (hard requirements) in Eq. (21) correspond to the stability requirements (gain and phase margins), whereas the minimisation goals  $f$  are the performance requirements listed in Table 1. The algorithms used to solve the optimisation problem in Eq. 21 are described in detail in [52–54] and are available as MATLAB implementations.

The controller architecture presented in this paper only represents the inner control loop used for the DLR HAP aircraft. Within the project, it will be extended by an outer loop autopilot, which enables energy management and trajectory tracking. In [55], for instance, the inner loop only consists of roll, pitch and yaw dampers, while a total energy control system and a total heading control system are used as outer loops.

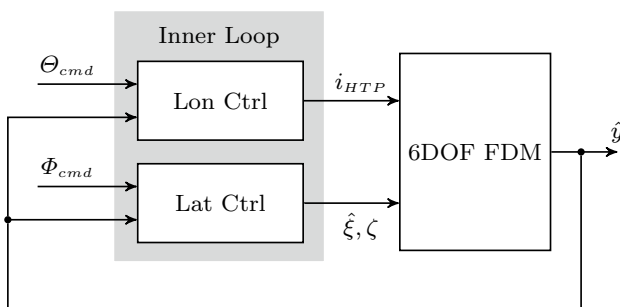


**Fig. 4** Baseline inner loop control architecture

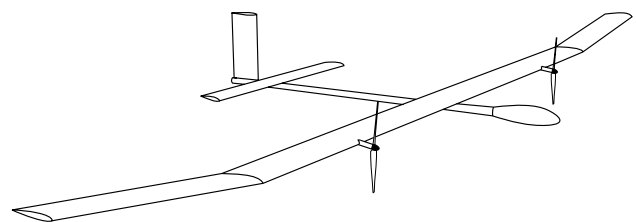


**Fig. 5** Sketch of the DLR HAP aircraft

**Table 2** Integral key parameters of the DLR HAP aircraft

Wing area		36 m <sup>2</sup>
Wing span		27 m
Dihedral	Inner wing	0°
	Outer wing	12°
Sweep		0°
Total mass		140 kg
Mass moments of inertia	$I_x$	2500 kg m <sup>2</sup>
	$I_y$	545 kg m <sup>2</sup>
	$I_z$	3000 kg m <sup>2</sup>
	$I_{xz}$	15 kg m <sup>2</sup>

**Table 3** Current approximate mass breakdown of the HAP aircraft

Elements	Portion (%)
Wing	21
Longerons	6
Tail	3
Solar generator	3
Propulsion system	6
Devices	13
Payload	4
Batteries	44

Note that the breakdown represents a demonstrator configuration with reduced solar generator surfaces, which is intended only for a single over-night flight

### 2.2.6 Resulting aircraft

Figure 5 shows a sketch of the resulting aircraft design obtained within the preliminary design phase.

Some integral key parameters of the aircraft are summarised in Table 2 and Table 3 lists the mass breakdown of the HAP aircraft.

As already stated in Sect. 1, the aim of the project *HAP* is to obtain, generate and publish knowledge about such aircraft. The DLR HAP aircraft is therefore not supposed to compete with other HAP designs. However, at this point a short comparison of the DLR HAP will be made with the Zephyr S, which is one of the most prominent aircraft of this type. The comparison is based on the information found in [15]. Besides the visible differences concerning the type of tailplane (the Zephyr S is equipped with a T-tail and the DLR HAP has a conventional tail) and the use of ailerons, the DLR HAP has a clearly higher total mass (140 kg) than the Zephyr S (65 kg), while their wing spans are in a similar order (27 m of the DLR HAP and 25 m of the Zephyr S). The DLR HAP aircraft has a wing area of 36 m<sup>2</sup> and the Zephyr S has a wing area of 28 m<sup>2</sup>. Therefore, the aspect

ratios of both aircraft are in a similar order. However, with 3,9 kg/m<sup>2</sup> in case of the DLR HAP aircraft and 2,3 kg/m<sup>2</sup> in case of the Airbus Zephyr S, the wing loadings differ significantly. As a consequence, the DLR HAP will have a lower energy efficiency. First, the DLR HAP aircraft's higher relative mass results from the components used. It is likely that the costs of some of the components, for instance the solar generator, played a more important role for the DLR HAP aircraft than for Zephyr S. Therefore, in some cases, heavier components might be used for the DLR HAP aircraft that, however, do not impede its usability as experimental HAP. Second, while designing the DLR HAP, a particular focus was put on risk mitigation during the flight test campaign. The use of ailerons leads to an additional weight penalty. In addition, the DLR HAP aircraft's structural sizing is supposedly more conservative, which would signify a higher structural stability.

## 3 Flight mechanical analyses

This section deals with flight mechanical analyses performed for the HAP aircraft within the preliminary design phase and with the design decisions made based on stability and control aspects.

It starts with a brief description of the initial flight envelope. Subsequently, this section presents the dynamic stability characteristics of the aircraft. Furthermore, a control surface design evaluation concept based on gust encounter simulations using the inner loop of the flight controller is presented. For this purpose, flight mechanical requirements are first defined that are used to justify the design choices. Second, exemplary gust encounter simulations are shown.

### 3.1 Initial flight envelope and nominal mission envelope

At this stage of the design phase, the flight envelope is initially defined based on aerodynamic characteristics and aeroelastic design assumptions before the envelope will further be restricted based on flight mechanical limitations. The altitude ranges from FL 0 to the aircraft's service ceiling of FL 800. The minimum allowable speed is limited by the associated altitude-dependent stalling speed  $V_S$ , which results from the aircraft's aerodynamic properties and mass. The upper speed limit is defined by the never-exceed-speed  $V_{NE}$ , which is deduced from the design diving speed. The design diving speed was defined based on engineering judgement and aeroelastic stiffness requirements.

In addition to the flight envelope, a nominal mission envelope is defined using nominal mission operation speed limits. Disregarding take-off and landing procedures, the aircraft is expected to perform its mission within this

envelope. Its limits are defined by two operation speeds. The first is the minimum operation speed  $V_{O,min}$ , deduced from the design manoeuvring speed, which is the lowest speed at which the aircraft can perform a pull-up manoeuvre with a load factor of 2. It was deduced by formal equations using the aircraft's aerodynamic properties and mass. The second is the maximum operation speed  $V_{O,max}$ , deduced from the design cruising speed, which was chosen such that a sufficient safety margin to  $V_{NE}$  is provided.

Table 4 summarises these characteristic envelope-defining airspeeds and gives the respective values at sea level.

With increasing altitude the characteristic true airspeeds increase in such a way that the respective equivalent airspeeds remain constant. The equivalent airspeed  $V_{EAS}$  relates to the true airspeed  $V_{TAS}$  at a given density  $\rho$  as

$$V_{EAS} = \sqrt{\frac{\rho}{\rho_0}} \cdot V_{TAS}, \quad (22)$$

with the density at sea level  $\rho_0$ . The same equivalent airspeed thus leads, independently of the flight altitude, to the same dynamic pressure. In addition, the stalling speed and the minimum operation speed further vary with the altitude due to Reynolds number effects. Thereby,  $V_S$  slightly increases and  $V_{O,min}$  slightly decreases at higher altitudes compared to their respective equivalent airspeed references.

### 3.2 Dynamic stability

As an unmanned aircraft operating beyond the line of sight of the pilot, the HAP aircraft is supposed to perform its missions fully autonomously. However, a proper design of the aircraft in terms of natural stability, provided that such a design is not accompanied by a too high weight or aerodynamic efficiency penalty, brings some reasonable benefits. Some of the most important advantages are:

- Higher success rate of the complete mission: An aircraft with natural dynamic stability is capable of maintaining a trimmed flight and to counteract disturbances up to a certain degree passively. In case of a temporary loss of communication with the aircraft, it can not be verified whether the flight controller and the flight management system are still operative. While for an unstable aircraft it is not possible to anticipate the aircraft's behaviour dur-

ing the communication loss, a naturally stable aircraft is more likely to simply continue the flight. Therefore, the standby time until the aircraft must be terminated can be extended.

- Less power consumption: An aircraft without natural stability must be stabilised using the flight control system. The associated control surface deflections lead to additional drag. Moreover, deactivating single actuators for a certain period of time in order to save power might be a valuable option, which can be especially advantageous during night. For naturally unstable aircraft, this option is limited to the actuators that are not needed for stabilisation.
- Better handling during the flight test campaign: During the flight test campaign the aircraft should, at the beginning, be piloted by a pilot test team until the single control loops are connected. The design of a naturally stable aircraft is thus beneficial with respect to a reduced risk of a loss of the aircraft.

For the dynamic stability investigations of the HAP, the flight dynamic model described in Sect. 2.2.4 is trimmed and linearised around the respective flight points of the flight envelope. Dynamic stability investigations are performed for the complete envelope. This way, it is ensured that the aircraft still shows a tolerable dynamic behaviour if it temporarily leaves the nominal operation envelope inadvertently, e.g. due to gust encounters. For all analyses the ground effect as well as the stall model are deactivated.

#### 3.2.1 Longitudinal modes

This section presents the HAP aircraft's longitudinal modes. The typical longitudinal modes are the phugoid mode and the short period mode. The classical phugoid mode is usually an oscillatory motion driven by an exchange of kinetic and potential energy. Aircraft drag characteristics and current airspeed most often have a strong influence on this mode. Typically, the short period is an oscillatory and strongly damped motion that involves mainly pitch rate and angle of attack, while altitude and airspeed just play a minor role.

In case of the HAP aircraft, the classification of the longitudinal modes as phugoid and short period can, strictly speaking, not be made without reservations. As will be shown later in this section, the aircraft indeed has a mode that has a similar shape as the classical phugoid but with a relatively high natural frequency. However, the higher-frequency mode also involves altitude and airspeed to a large extent, and thereby differs from the classical short period.

Figure 6, showing simulation time histories, demonstrates this circumstance. For the simulations, the aircraft was trimmed in a stationary horizontal flight at 10 m/s equivalent airspeed and different altitudes. Compared to the trim values,

**Table 4** Characteristic airspeeds of the HAP aircraft at sea level

$V_S$	6.5 m/s
$V_{O,min}$	9.0 m/s
$V_{O,max}$	11.0 m/s
$V_{NE}$	15.5 m/s

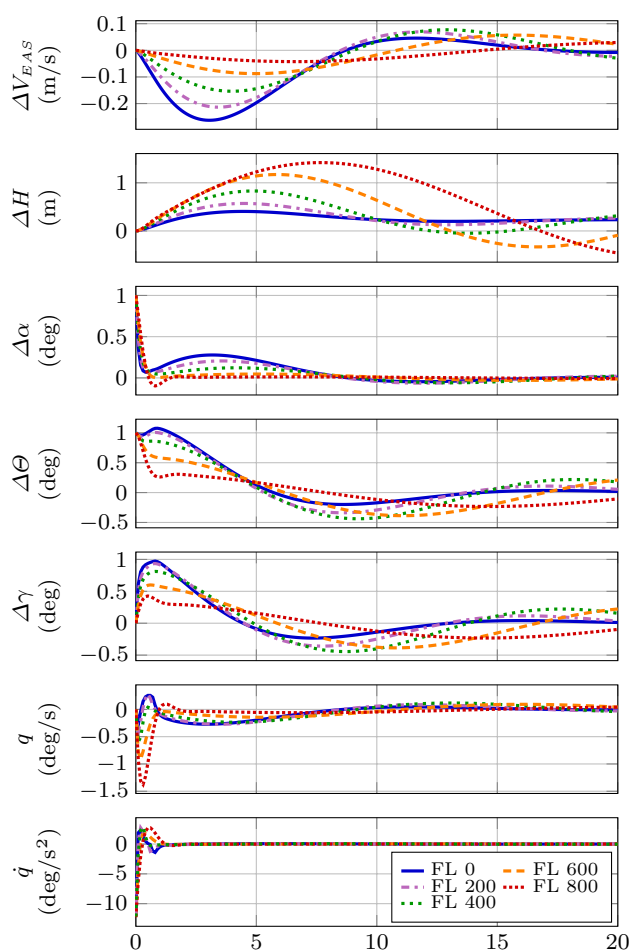


**Fig. 6** Simulations with an initial angle of attack and pitch angle perturbation at 10 m/s equivalent airspeed and different altitudes

an initial perturbation of  $1^\circ$  is applied to the angle of attack and the pitch angle. At the same time, the control surface deflections and thrust inputs are kept fixed at the trimmed values. The simulation is then run without any additional control surface or thrust inputs.

As illustrated, the initial angle of attack perturbation of  $1^\circ$  decreases rapidly. However, this is mainly associated with an increase of the flight path angle  $\gamma$  rather than with a decrease of the pitch angle  $\Theta$ . Hence, the aircraft starts to climb first. After a longer time, i.e. after around 5 seconds, the aircraft stops climbing and finally, the pitch angle perturbation has mostly vanished. The aircraft also shows an initial pitch reaction that subsides after a short time. Along with an increasing altitude, this initial climb reaction becomes less distinct. Altogether, the mode differs from the classical short period eigenmode as it involves altitude and airspeed changes to a large extent. Therefore, in this paper the longitudinal modes will be called “short period”-type and “phugoid”-type modes. The latter is visible in the

Fig. 6 through the low frequency oscillations with a period of around 20–30 seconds, depending on the altitude.

Figure 7 shows the poles of the associated longitudinal modes for the HAP aircraft in the complete flight envelope. Part 7a illustrates the pole plot of the “phugoid”-type mode with the  $x$ -axis representing the real parts and the  $y$ -axis representing the imaginary parts. A negative sign of the real part signifies a stable dynamic motion. The results are provided for different altitude levels ranging from FL 0 to FL 800 and several different equivalent airspeeds for each altitude. Flight shape-dependent aerodynamic derivatives are available for four nodes, being the different airspeeds that define the envelope, namely  $V_S$  (solid circle marker),  $V_{O,min}$  (solid square marker),  $V_{O,max}$  (solid diamond marker) and  $V_{NE}$  (solid star marker). Derivatives for intermediate airspeeds are obtained using linear interpolation. To give an idea of these flight shapes, Fig. 8 depicts the spanwise elastic deformation of wing and HTP in  $z$ -direction for different values of the equivalent airspeed.

Note that this way of modelling the quasi-stationary aeroelastic effects has an impact on the results shown in this section. It adds a gradient to the derivatives with respect to the equivalent airspeed. These gradients are constant between two nodes, e.g.,  $V_S$  and  $V_{O,min}$  and change as soon as the flight point is located between a different combination of nodes, e.g.,  $V_{O,min}$  and  $V_{O,max}$ . This effect is particularly perceivable in case of the “phugoid”-type mode, since this motion involves the airspeed to a significant extent. It can be observed in Fig. 7a, showing that the effect leads to a slight shift of the poles when the airspeed surpasses  $V_{O,min}$ .

Part 7c shows, for the purpose of a better readability, only the real parts of this mode across the equivalent airspeed. The full squares represent the flight points that are located within the nominal operation envelope. As shown, at higher altitudes the equivalent airspeed  $V_S$  increases slightly and the equivalent airspeed  $V_{O,min}$  decreases. This is due to Reynolds number effects.

For a better understanding of these figures, it is helpful to understand that an increase of the equivalent airspeed at a constant altitude signifies an increase in dynamic pressure and a change in flight shape while an increase in altitude at constant equivalent airspeed signifies an increase in true airspeed and a reduction of density.

The “phugoid”-type mode of the HAP aircraft is stable and oscillatory at low airspeeds and comparatively strongly damped at low altitudes. Damping decreases along with the altitude but the mode is still damped at FL 800. At all altitudes, the poles approach the real axis with increasing airspeed. At FL 0 and FL 200, this even leads to this mode translating into two aperiodic modes. This aperiodic behaviour results from the aeroelastic HTP effectiveness in combination with the low drag of the aircraft. At higher dynamic pressures the resulting lift curve slope of the HTP is reduced

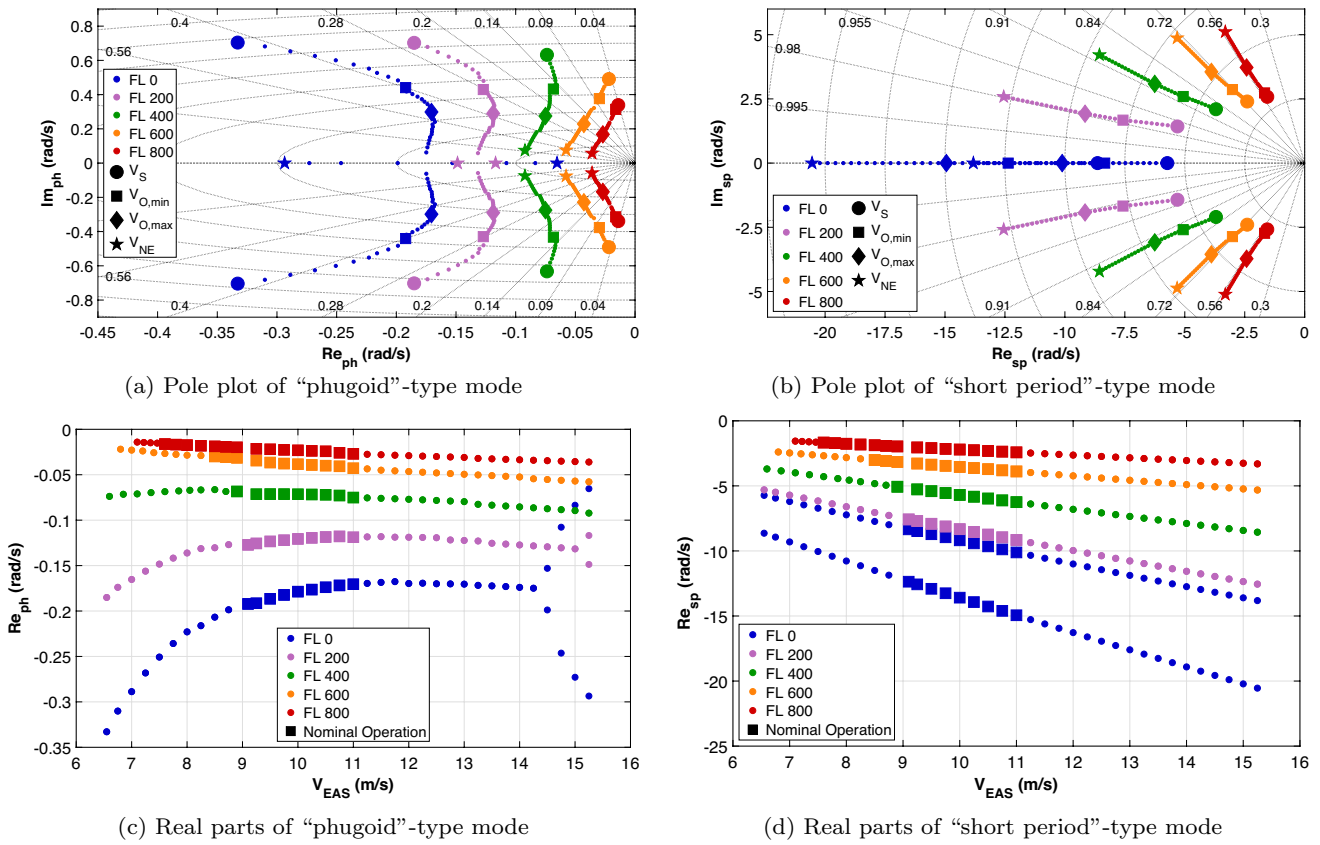


Fig. 7 Poles of the longitudinal modes

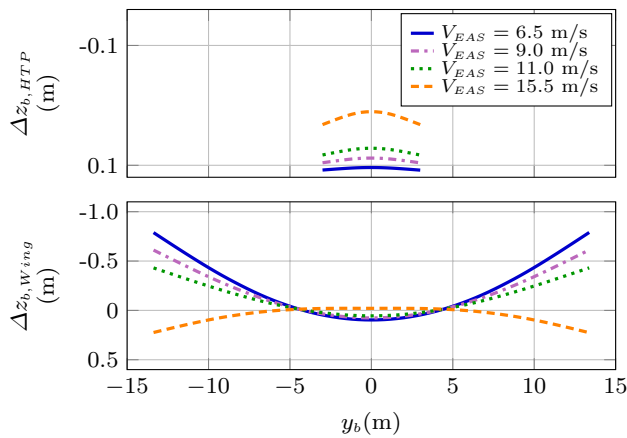


Fig. 8 Elastic deformation of wing and HTP in  $z$ -direction for different equivalent airspeeds, respectively the characteristic airspeeds at sea level

due to a bending of the fuselage. A change in airspeed, thus, results in a change of HTP effectiveness.

Figure 7b shows the eigenvalues of the second longitudinal mode. This higher-frequency mode is similar

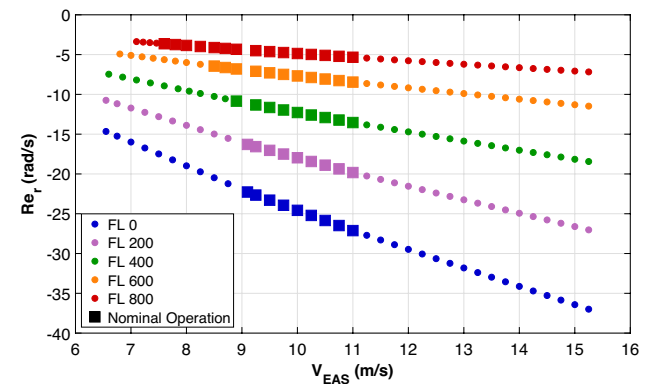
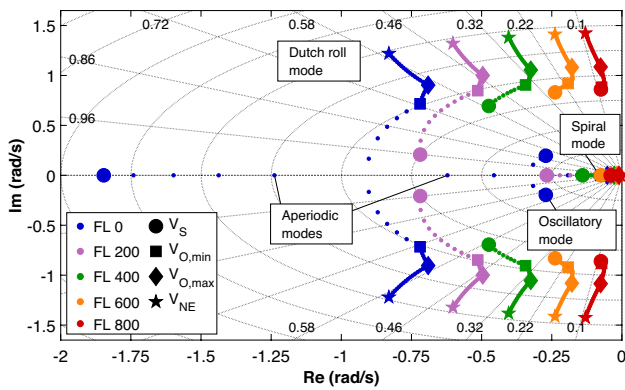


Fig. 9 Real parts of the roll mode

to the typical short period mode, but it additionally involves altitude and airspeed to a significant extent. The associated poles of the HAP aircraft indicate two quickly decaying aperiodic modes at FL 0. At higher altitudes, this mode exhibits an oscillatory character but it is still comparatively strongly damped. Part 7d depicts the associated real parts. An increase in equivalent airspeed



**Fig. 10** Lateral-directional modes; Dutch roll, spiral and, at FL 0 and low airspeeds, non-classical modes

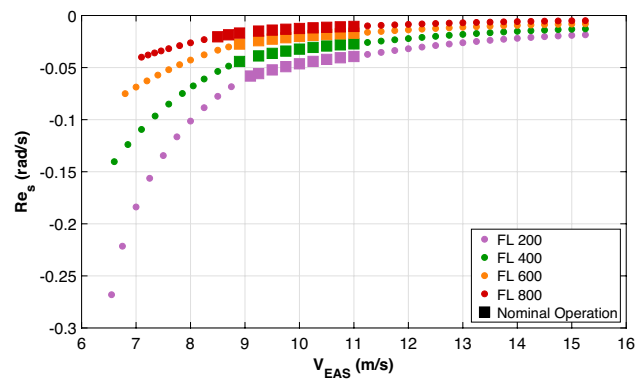
and thereby of dynamic pressure has a stabilising effect on all modes, both the aperiodic and the oscillatory ones.

### 3.2.2 Lateral-directional modes

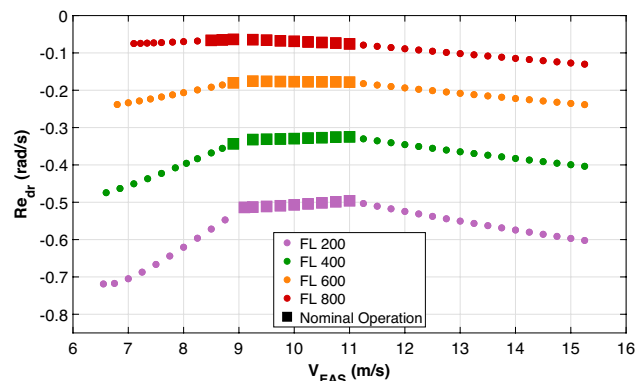
This section deals with the aircraft’s lateral-directional modes. Figure 9 shows the real parts of the aperiodic roll motion. As expected because of the HAP aircraft’s high aspect ratio, this mode is quickly decaying at all points of the flight envelope. An increase of altitude has a destabilising effect on the roll motion due to the lower air density, while an increase in equivalent airspeed has a stabilising effect.

The HAP aircraft has a Dutch roll and a spiral mode at most points of the flight envelope. At FL 0 and at very low airspeeds, however, it exhibits non-classical oscillatory and aperiodic eigenmodes. Figure 10 shows the respective poles for the HAP aircraft. In addition, Fig. 11 depicts the associated real parts. Figure 11a shows the spiral real parts for all altitudes except FL 0. The classical aircraft spiral mode is a slow aperiodic motion that involves mainly roll, yaw and sideslip angle. For the HAP aircraft, the spiral mode, where applicable, is decaying for all airspeeds and all altitudes. As shown, an increase in altitude has a slight destabilising effect on the spiral. A reduction of the airspeed, in turn, has a stabilising effect. This can mainly be attributed to the flight shapes. At low airspeeds, the elastic wing dihedral increases, which has an effect on the induced rolling moment due to a sideslip angle. The higher the dihedral, the stronger the left roll moment reaction as a response to a right sideslip angle gets. This aircraft behaviour, represented by the derivative  $C_{l\beta}$ , has a stabilising effect on the spiral.

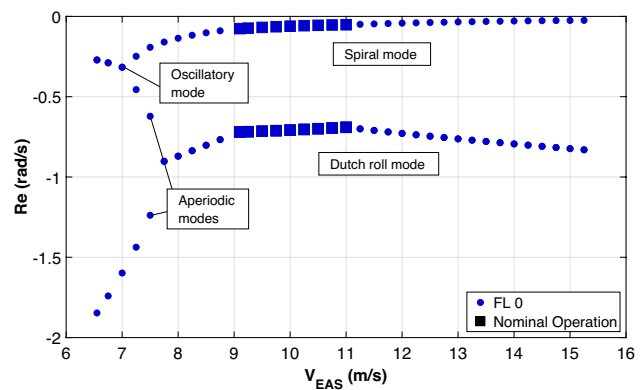
The Dutch roll mode typically is a weakly damped oscillatory motion that includes excitations both around the roll and the yaw axes. As shown by Fig. 10, the HAP aircraft’s Dutch roll is stable in the complete flight envelope and oscillatory at all altitudes except at FL 0 for very low airspeeds.



(a) Spiral real parts



(b) Dutch roll real parts



(c) Real parts of Dutch roll, spiral and non-classical modes

**Fig. 11** Lateral-directional real parts; Dutch roll, spiral and further non-classical modes

The Dutch roll is reasonably damped at low altitudes. At higher altitudes, damping of the rotational rates decreases due to the lower air density which leads to a reduction of Dutch roll damping. Nevertheless, at the most critical point of the flight envelope, being  $V_S$  at FL 800, the Dutch roll is still slightly damped. Figure 11b shows the associated Dutch roll real parts.

At FL 0 and at very low airspeeds, Dutch roll mode and spiral mode start to interact and to exhibit non-classical

modes instead, as shown by Fig. 10. Figure 11c shows the associated real parts. At 7.5 m/s equivalent airspeed, respectively true airspeed, the Dutch roll mode is not oscillatory any more. Instead, the aircraft shows two aperiodic modes. While further reducing airspeed, the pole of one of these modes moves to the left side and the other one moves to the right side into the direction of the spiral mode pole, as shown by Fig. 10. At 7.0 m/s the pole of the aperiodic mode that moved to the right reaches the spiral pole, which leads to the forming of a new oscillatory mode. The new oscillatory mode is a strongly damped motion with rather small natural frequency. Figure 12 shows the eigenvectors of these lateral-directional modes for some selected airspeeds at FL 0. The eigenvectors are normalised in each case.

Figure 12a shows the lateral-directional eigenvectors, excluding the roll mode, for  $V_{O,min}$  at FL 0. At this flight point, the aircraft still has a spiral and a Dutch roll mode. The Dutch roll mode particularly involves yaw rate, yaw angle and sideslip angle to a large extent, while the roll rate and roll angle play a rather subordinated role. The spiral mode mostly involves the yaw angle and also sideslip angle, yaw rate and roll angle to a smaller extent.

At 7.5 m/s, the aircraft does not have a classical Dutch roll mode anymore. Instead, there are two aperiodic modes. Figure 12b shows these aperiodic modes together with the yet existent spiral mode. As shown, the first aperiodic mode has a similar shape as the Dutch roll mode at  $V_{O,min}$ . The second aperiodic mode then almost exclusively involves sideslip angle, yaw rate and yaw angle. The spiral mode shape also changes in comparison to  $V_{O,min}$ . In doing so, its shape becomes more similar to that of the second aperiodic mode.

At  $V_S$ , the second aperiodic mode and the spiral mode have formed an oscillatory mode (Fig. 12c). It has a similarity to the Dutch roll mode at  $V_{O,min}$ . However, in comparison, the yaw rate is less involved and the sideslip angle is the predominant state in this mode. The aperiodic mode involves, aside from the sideslip angle, the yaw and roll rates to a relatively large extent and thus forms a kind of a turning mode.

### 3.3 Gust encounter simulations

Unmanned high-altitude platforms usually are operated as experimental aircraft. Classical flight mechanical certification requirements, such as in the EASA CS-22 [56] certification standards, for the most part are not applicable for such a configuration or would turn its application unrealistic. The JARUS guidelines on SORA only provide few guidelines that could directly be converted into aircraft flight dynamic requirements. In addition, typical handling qualities criteria like those that can be found in MIL-STD-1797A [57] for manned aircraft, which are often used to extract and

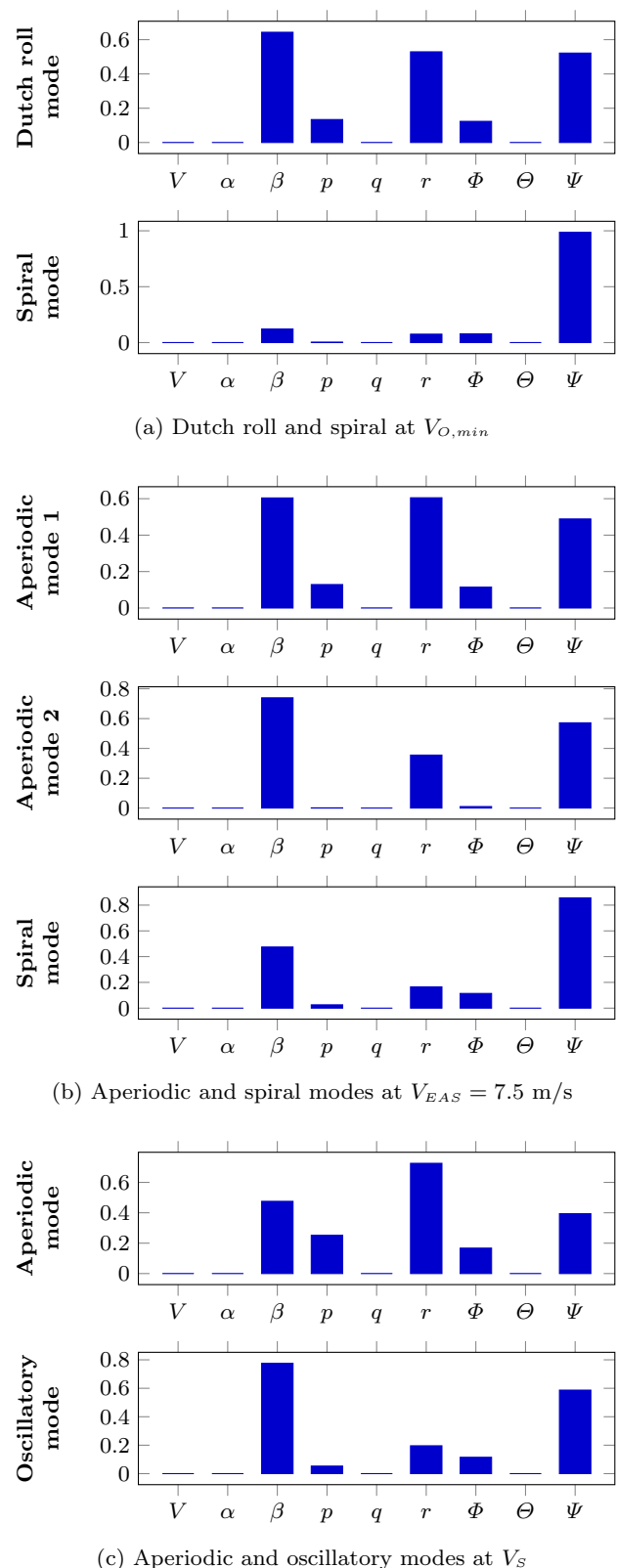


Fig. 12 Lateral eigenvectors at FL 0



derive aircraft characteristics, are not available for HAP aircraft. In absence of these certification requirements, new requirements need to be defined that are derived from mission assumptions for the aircraft itself, critical scenarios during its life time, and also from test range demands and constraints.

As already pointed out in Sect. 1, a significant number of HAP aircraft have already crashed during flight tests experiments. Their low airspeed and high flexibility make them particularly vulnerable to disturbances and their comparatively low agility hinders timely and effective countermeasures. In order to reduce the risk of an accident during the flight test campaign in the project *HAP* due to atmospheric turbulences and to facilitate manual piloting tasks, it has been decided that a demonstrator configuration will be used for the flight tests. This demonstrator configuration is supposed to be, from a flight physical point of view, as similar to the final aircraft as possible. Whether ailerons are necessary to control the aircraft under all circumstances needs to be investigated. The demonstrator will be equipped with ailerons but this might not be the case for the final configuration.

The aircraft and its control surfaces shall be designed in such a way that, at all altitudes and at airspeeds between  $V_{O,min}$  and  $V_{O,max}$ , as a result of

- (a) a vertical gust encounter in both directions,
- (b) a lateral gust encounter,
- (c) an encounter with a pair of a vertical and a lateral gust,

using the control surfaces to counteract, the

- (a) airspeed does not fall below  $V_S$ .
- (b) airspeed does not exceed  $V_{NE}$ .
- (c) aircraft is able to return to a stabilised flight condition.

**Fig. 13** Requirements on the HAP's control surfaces

**Table 5** Gust magnitudes in m/s for different altitudes and gust wavelengths as considered in the simulations

		Gust wavelengths (m)				
		9.0	33.5	58.0	82.5	107.0
Altitude	FL 0	4.37	5.44	5.96	6.32	6.61
	FL 200	4.64	5.78	6.33	6.72	7.01
	FL 400	5.37	6.68	7.33	7.77	8.11
	FL 600	6.07	7.56	8.28	8.78	9.17
	FL 800	5.19	6.46	7.08	7.51	7.84

### 3.3.1 Definition of control surface requirements

A multitude of requirements have been defined for the HAP aircraft. However, this paper only focusses on the requirement that addresses the HAP's control surfaces. While the control surface design is usually driven by the mission-based need for agility, for the HAP aircraft those needs are not the most restrictive since the HAP aircraft is supposed to operate in a restricted area. Instead, its low airspeed makes it particularly vulnerable to gust encounters. Therefore, the control surfaces need to be sized such that they can be used to counteract reactions to gusts and to prevent a loss of the aircraft (Fig. 13). The associated requirement reads:

This requirement solely addresses the nominal operation envelope of the aircraft. Date and time for take-off and landing of the HAP need to be chosen with the utmost care with respect to weather conditions, anyway. The design gusts are based on those defined in the EASA CS-25 [58]. However, the gust magnitudes are reduced by a factor of 0.5, which is expected to be in accordance with the HAP's overall service time. More background information on this magnitude reduction is provided by [35]. Table 5 shows the resulting gust magnitudes.

As shown, the gust velocities are of a similar order as the HAP's cruise speed. Therefore, significant aircraft reactions cannot be avoided. The only aim in case of gust encounters is to use the control surfaces to prevent the HAP from entering a flight condition that it cannot be recovered from. Note that this requirement only addresses control surface needs. Therefore, no headwind or tailwind gusts are applied, which would be more critical with respect to airspeed deviations. However, in this regard, a change of the thrust settings would be the most effective and would need to be applied. For the same reasons, no altitude change restrictions are defined in this requirement. Furthermore, note that no restrictions on maximum rotational rates and accelerations are included in this requirement since these are covered by the gust and manoeuvre loads analyses.

### 3.3.2 Simulation results

This section demonstrates the evaluation of the afore-mentioned gust encounter requirement in the complete envelope.

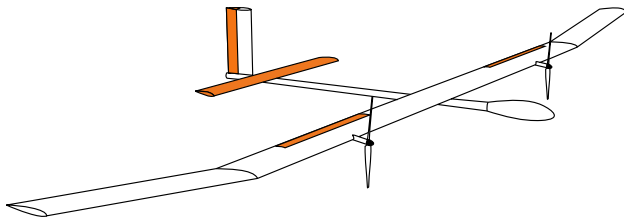


**Fig. 14** Sketch of the HAP aircraft with control surfaces emphasised with orange colour

Figure 14 shows the HAP aircraft along with its control surfaces that are to be evaluated. The aircraft is equipped with an all moving stabiliser, which is used for trimming and for applying pitch commands, a rudder and, as discussed above, ailerons. The high flexibility of the aircraft causes a decrease of aileron effectiveness along with the spanwise position, due to the local pitching moment caused by the aileron deflection. This is a well-known effect that also affects other categories of aircraft such as jet aircraft at high Mach numbers and possibly could lead to aileron reversal [59]. As a consequence, the ailerons of the DLR HAP aircraft need to be placed relatively close to the aircraft centreline to achieve a compromise between effectiveness and lever arm.

Figure 15 shows the time histories of an application of the requirement exemplarily for a pair of a downwind gust and a lateral gust at two different flight points. The gusts are varied in wavelength and maximum speed, whereas the variation is done simultaneously for both gusts. The quasi-stationary 6DOF model described in Sect. 2.2.4 is used for the simulations with the stall model activated and the ground effect model deactivated. This signifies that the lateral components of the gust are supposed to act on VTP and wing simultaneously while for vertical and horizontal components the transport lag takes effect. Here, part 15a shows the results at FL 0 and at airspeed  $V_{O,min}$ . Five simulations with different wavelengths are illustrated together in the same plots. They are distinguishable by colour and style of the lines.

The control surface deflection commands are produced by the inner loop of the flight controller described in Sect. 2.2.5. As shown, the gust speeds are of a similar magnitude as the airspeed of the aircraft. As a consequence, the aircraft shows severe reactions. The stabiliser input  $i_{HTP}$  is even temporarily at its deflection limit while reducing the aircraft response. The lateral component of the gust is counteracted using the ailerons to decrease the roll rate  $p$  and using the rudder to turn into the wind to reduce the sideslip angle  $\beta$  and thereby  $v_{W,b}$ . This can also be observed in the longitudinal body-fixed wind component  $u_{W,b}$ , which also shows the characteristic gust shape even though no longitudinal gust was applied. It can be observed that the airspeed  $V_{TAS}$  gets near the defined lower limit but does not violate it.

Part 15b shows the simulation results at FL 600 and at airspeed  $V_{O,max}$ . As shown, due to the comparatively high airspeed (for this aircraft type), the control surface deflections become less relevant. Instead, the pure aircraft reaction due to the gust is predominant. As a consequence, the resulting rotational rates are higher in this case than in the other case, where the airspeed is sufficiently low such that the control surfaces can be used more effectively to counteract the responses. The pitch rate forms an exception here because the stabiliser was at its limit at FL 0 and  $V_{O,min}$ . Therefore, the potential to reduce the resulting pitch rate could not be used to its fullest. In return, the resulting deviations of airspeed and the aerodynamic angles are lower than at FL 0 and  $V_{O,min}$  for most gust wavelengths. All in all, the case at FL 600 and  $V_{O,max}$  is more relevant for loads analyses than for the control surface evaluation.

Given that the wind speeds are in the same order of magnitude as the airspeed of the HAP aircraft, it might not seem intuitive that the aerodynamic angles, with maximum values for  $\alpha$  of around  $\pm 10^\circ$  and for  $\beta$  of around  $\pm 20^\circ$  are comparatively low. It must be noted here, that the HAP aircraft is extremely light and therefore tends to move along with the wind rather than to show dynamic reactions. However, for the sake of better perceptibility, the flight path velocity components are not presented here.

In these simulations, actuators are modelled as second-order systems with rate limits of  $\pm 20^\circ/\text{s}$ . This value represents the worst case of the aerodynamic load-dependent rate limits and is therefore very conservative.

In all gust encounter simulations, the HAP aircraft was able to return to a stabilised flight condition. Finally, Fig. 16 shows the minimum and maximum values that occurred during these simulations in the complete envelope and for all gusts. The first plot shows the values for equivalent airspeed along with the respective limits. Note again, that the stalling speed, which forms the lower limit, is altitude-dependent due to Reynolds number effects. The equivalent airspeed never leaves the boundaries, even though the minimum values are close to the lower limits a couple of times. Here, the additional use of thrust to counteract the gusts would be beneficial to further reduce the airspeed deviations and make the gust encounters less critical.

The second plot illustrates the angle of attack. Relatively large values are obtained that already lead to main wing stall. However, as demonstrated by the sixth plot, the maximum and minimum HTP lift coefficients are still moderate; therefore, the aircraft is always able to return from these conditions. This can be attributed to the dynamic HTP angle of attack caused by the pitch rates.

As already mentioned, the altitude deviations, particularly due to vertical gusts, are very high if only the control surfaces are used to counteract the gusts. This is shown by the

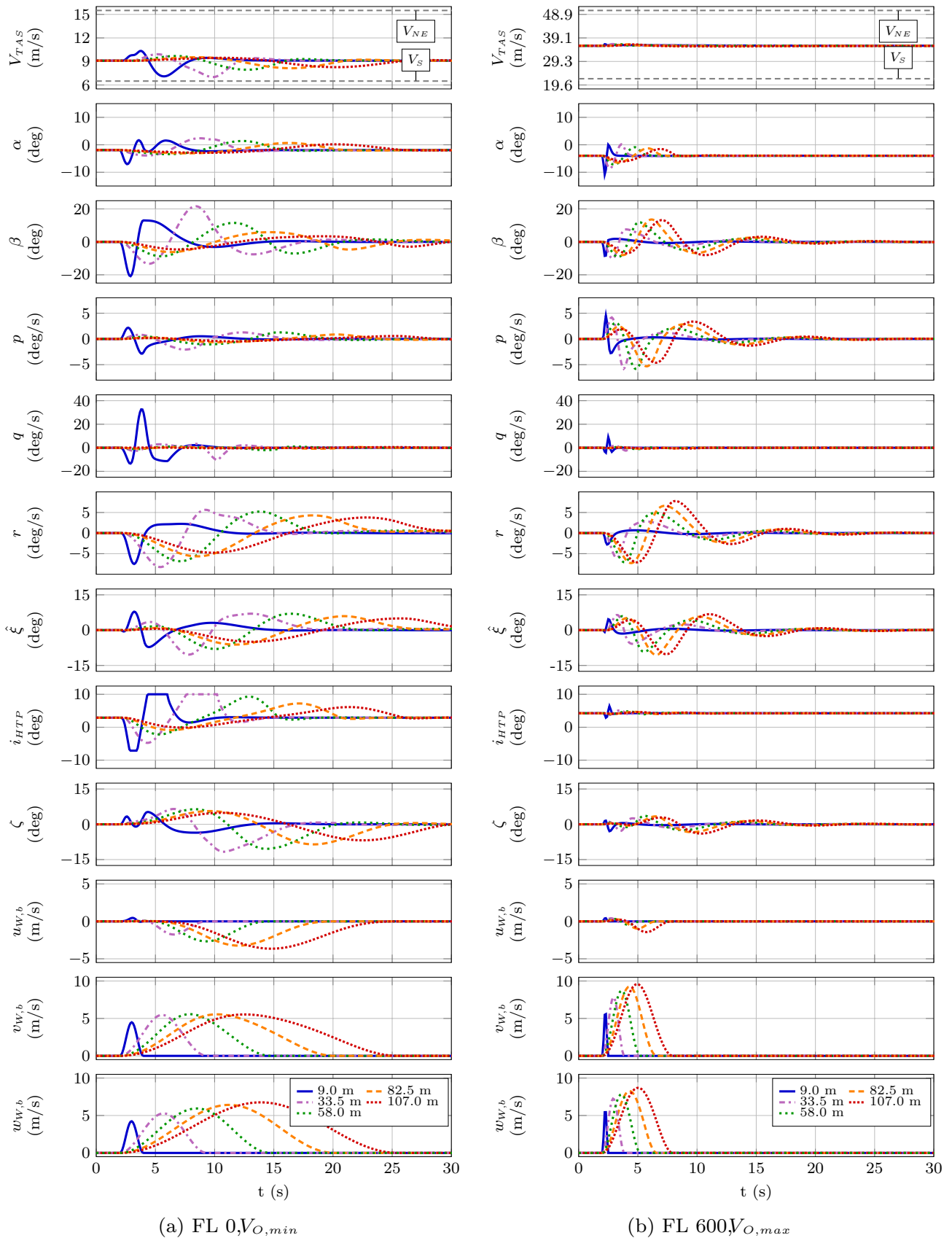
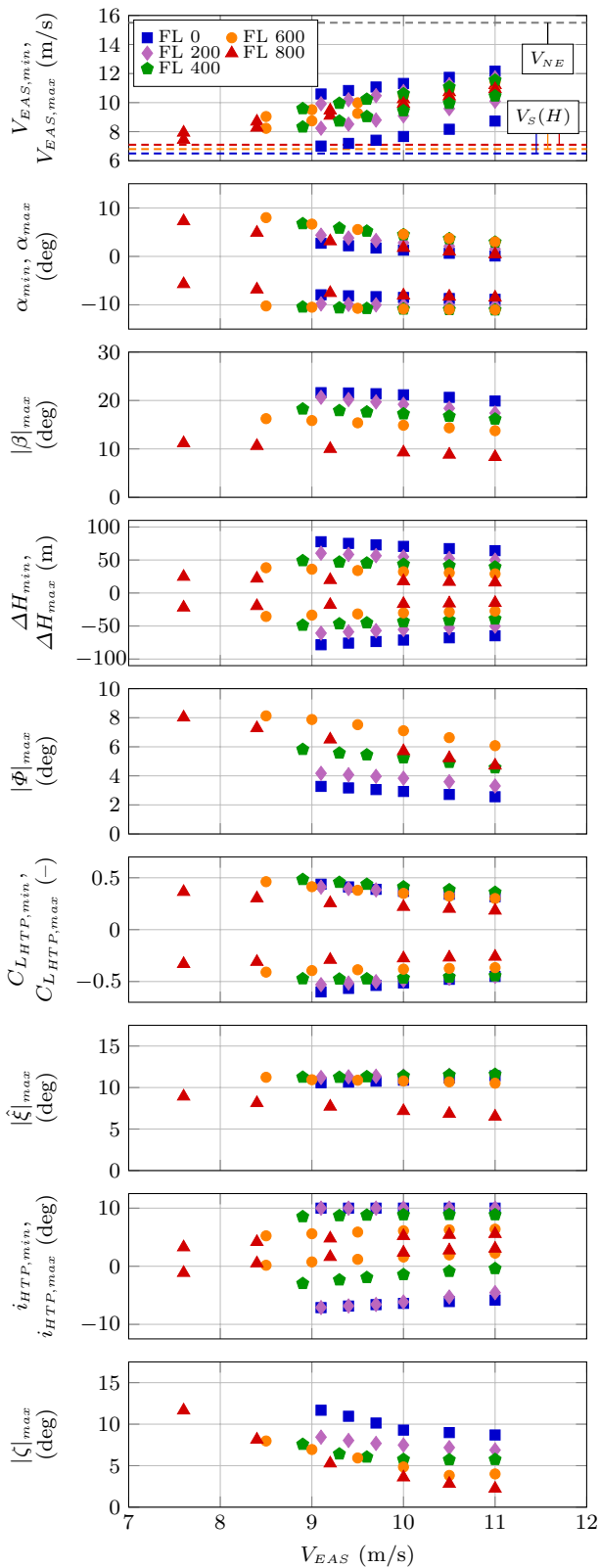


Fig. 15 Simulation of encounters with several pairs of downwind and lateral gusts at FL 0 and  $V_{O,min}$  and at FL 600 and  $V_{O,max}$  using the inner loop of the flight control system



**Fig. 16** Minimum and maximum values occurring during gust encounter simulations

fourth plot. The large absolute values illustrate the need to include thrust inputs in case of gust encounters.

To conclude, the control surfaces used for the gust rejection simulations are adequate, since the afore-defined requirement is met using them.

## 4 Conclusion

The aim of this paper was to present the flight mechanical analyses performed within the preliminary design phase for the HAP aircraft that is currently under development by the DLR in the context of the project HAP. Therefore, the paper gave an overview of the different disciplines involved in the preliminary design and presented some of the associated methods and results. Subsequently, different flight dynamic analyses using a non-linear 6DOF flight dynamic model that included the results of the other disciplines were shown.

The first analysis comprised a detailed investigation of the flight dynamic modes in the complete flight envelope. All eigenmodes proved to be naturally stable. In the longitudinal motion, the HAP aircraft had two eigenmodes that were oscillatory at nearly all flight points and somewhat similar to the classical short period and phugoid modes. However, the “short period”-type mode involved altitude and airspeed to a significant extent. As a consequence, a small angle of attack perturbation already caused the aircraft to climb or descent significantly. A transition of the “phugoid”-type mode from a stable oscillatory mode to two stable aperiodic modes at higher airspeeds was observed. It was mainly driven by low drag of the aircraft and reduced HTP effectiveness due to aeroelastic effects. At FL 0 and very low airspeeds, the Dutch roll translated into two aperiodic modes, one of which approached the spiral poles forming a new oscillatory motion. Altogether, due to the large range of flight points, particularly in terms of the altitude, the poles were widespread in the complete envelope.

It should be noted that no flexible mode dynamics were included in the flight dynamic model. Instead, a quasi-stationary approach was used. Due to the high flexibility of the aircraft it may be assumed that some of the lower frequency modes are in the same frequency range as the rigid body dynamics. An extension of the model by the flexible mode dynamics and a re-analysis of the HAP eigenmodes is therefore highly recommendable to investigate coupling effects.

The second analysis dealt with a control surface evaluation based on gust encounter simulations. On terms of a newly defined requirement, the HAP aircraft was subjected to vertical and lateral gusts, as well as to a pair of both, in the complete envelope. The gusts were varied in speed

and wavelength. Control surface deflection commands were set by the inner loop of the flight controller to counteract the aircraft responses. The control surfaces were required to be designed such that the aircraft did not enter a non-recoverable flight condition. This indeed was not the case in the complete operational envelope. Gust definitions were mainly based on the CS-25 specifications that address larger passenger aircraft but with a gust magnitude reduction by a factor of 0.5. It is possible that for the HAP aircraft the minimum wavelength might need to be reduced to a domain where no gust spectrum data is available. However, the performed simulations give an impression of how the issue of control surface sizing can be treated for HAP aircraft. In sum, the obtained control surfaces are likely to be adequate to counteract the responses of lower frequency gusts.

## 5 Future work

The obtained results presented in this paper are used within the further course of the project *HAP*. From a flight mechanical point of view, several steps still need to be performed in the project. Here, one of the most important steps is to integrate the flexible mode dynamics into the flight dynamic model instead of respecting flexibility in a quasi-stationary form using interpolation between different flight shapes. Subsequently, the analyses described in this paper should be repeated to investigate e.g. coupling effects between the rigid body dynamics and the flexible dynamics. Finally, the aircraft must be manufactured and the flight test campaign needs to be thoroughly prepared and executed.

**Funding** Open Access funding enabled and organized by Projekt DEAL.

**Open Access** This article is licensed under a Creative Commons Attribution 4.0 International License, which permits use, sharing, adaptation, distribution and reproduction in any medium or format, as long as you give appropriate credit to the original author(s) and the source, provide a link to the Creative Commons licence, and indicate if changes were made. The images or other third party material in this article are included in the article's Creative Commons licence, unless indicated otherwise in a credit line to the material. If material is not included in the article's Creative Commons licence and your intended use is not permitted by statutory regulation or exceeds the permitted use, you will need to obtain permission directly from the copyright holder. To view a copy of this licence, visit <http://creativecommons.org/licenses/by/4.0/>.

## References

1. Airbus Defence and Space, Airbus Zephyr, Solar High Altitude Pseudo-Satellite flies for longer than any other aircraft during its successful maiden flight, Press Release, (8th August 2018)
2. D'Oliveira, F., Melo, F., Devezas, T.: "Highaltitude platforms - present situation and technology trends," vol. 8, (August 2016), pp. 249–262. <https://doi.org/10.5028/jatm.v8i3.699>
3. Runge, H., Rack, W., Ruiz-Leon, A., Hepperle, M.: "A Solar Powered HALE-UAV for Arctic Research," 1st CEAS European Air and Space Conference, (September 2007)
4. Mohammed, A., Mehmood, A., Pavlidou, F.-N., Mohorcic, M.: The Role of High-Altitude Platforms (HAPs) in the Global Wireless Connectivity. Proceedings of the IEEE **99**, 1939–1953 (2011). <https://doi.org/10.1109/JPROC.2011.2159690>
5. National Aeronautics and Space Administration, Dryden Flight Research Center, Solar-Powered Research and Dryden, NASA Facts: FS-1998-10-0054 DFRC, available online at [https://www.nasa.gov/centers/dryden/pdf/120308main\\_FS-054-DFRC.pdf](https://www.nasa.gov/centers/dryden/pdf/120308main_FS-054-DFRC.pdf), (1998)
6. National Aeronautics and Space Administration, Environmental Research Aircraft and Sensor Technology (ERAST), NASA Armstrong Fact Sheet: FS-020-DFRC, available online at <https://www.nasa.gov/centers/armstrong/news/FactSheets/FS-020-DFRC.html>, (28th February 2014)
7. Ross, H.: "Fly Around the World with a Solar Powered Airplane," in Technical Soaring, An International Journal, vol. 32, (September 2008). <https://doi.org/10.2514/6.2008-8954>
8. Nunez, C.: "Solar Impulse 2 Completes Trip Around World, Demonstrates Clean Energy and Aviation," National Geographic, (25th July 2016), Available online at <https://www.nationalgeographic.com/news/2016/07/solar-impulse-completes-trip-around-world-abu-dhabi-solar-power-airplane/>
9. Stevens, P.: "Zephyr: Pioneering the Stratosphere, ZP-PN-0039v2.0," (25th February 2019), Presentation, available online at <https://aaus.org.au/wp-content/uploads/2019/03/Paul-Stevens-Airbus-at-AAUS-Exploring-an-Unmanned-Future-Conference-20190225.pdf>
10. Malewar, A.: "Airbus's solar-powered Zephyr UAS crashes after a 64-day flight," Inceptive Mind, (25th August 2022), Available online at <https://www.inceptivemind.com/airbus-solarpowered-zephyr-uav-crashes-64-day-flight/25969/>
11. Noll, T., Brown, J., Perez-Davis, W., Ishmael, S., Tiffany, G., Gaier, M.: Investigation of the Helios Prototype Aircraft Mishap, NASA-Helios Mishap Investigation Board, (16th January 2004)
12. National Transportation Safety Board, Aviation Accident Report-Accident DCA15CA117, Titan Solara 50, N950TA, (1st May 2015)
13. National Transportation Safety Board, Aviation Accident Report - Accident DCA16CA197, Facebook Aquila, N565AQ, (28th June 2016)
14. Australian Transport Safety Bureau, Aviation safety investigations & reports -AO-2019-056, Airbus Zephyr, (28th September 2019)
15. Gonzalo, J., Lopez, D., Domínguez Fernández, D., García, A., Escapa, A.: On the capabilities and limitations of high altitude pseudosatellites. Progress. Aerospace. Sci. **98**, 37–56 (2018). <https://doi.org/10.1016/j.paerosci.2018.03.006>
16. Joint Authorities for Rulemaking of Unmanned Systems, JARUS guidelines on Specific Operations Risk Assessment (SORA), Edition 2.0, Final Release, (30th January 2019)
17. European Union Aviation Safety Agency, Acceptable Means of Compliance (AMC) and Guidance Material (GM) to

- Commission Implementing Regulation (EU) 2019/947, Issue 1, Annex I to ED Decision 2019/021/R, (9th October 2019)
18. Hepperle, M., Runge, H.: "HALE platforms-a feasibility study," DLR, German Aerospace Center, Report of the Institute of Aerodynamics and Flow Technology, IB 124-2007/11, (December 2007), Available online at <https://elib.dlr.de/54341/>
  19. BAE Systems, Ground-breaking solar powered unmanned aircraft makes first flight, Available online at <https://www.baesystems.com/en/article/ground-breaking-solar-powered-unmanned-aircraft-makes-first-flight>, (Retrieved July 2022)
  20. UAVOS, UAVOS Flight Tests ApusDuo Stratospheric Platform, Available online at <https://www.uavos.com/uavos-flight-tests-apusduo-stratospheric-platform/>, (Retrieved July 2022)
  21. Drela, M.: Flight vehicle aerodynamics, The MIT Press, (2014)
  22. Drela, M., Youngren, H.: AVL user primer, Available online at <https://web.mit.edu/drela/Public/web/avl/>
  23. Eppler, R., Somers, D.: "A computer program for the design and analysis of low-speed airfoils," NASA, NASA TM 80210, (1980)
  24. XFOIL User's Guide, Web site at <https://web.mit.edu/drela/Public/web/xfoil/>
  25. XFLR5 User's Guide, Web site at <https://www.xflr5.tech/xflr5.htm>
  26. Betz, A.: "Schraubenpropeller mit geringstem Energieverlust (in English: Screw Propellers of Lowest Energy Loss)," in Nachrichten der Königlich-Physikalische Klasse, (1919), pp. 193–217
  27. Prandtl, L., Betz, A.: "Vier Abhandlungen zur Hydrodynamik und Aerodynamik (in English: Four Papers on Hydrodynamics and Aerodynamics)," Kaiser-Wilhelm-Gesellschaft Göttingen, Germany, pp. 68–92, (1927)
  28. Larrabee, E.: Practical design of minimum loss propellers. Business. Aircraft. Meeting. Exposition., Paper 790585, 68–92 (1979)
  29. Adkins, N., Liebeck, R.H.: Design of Optimum Propellers. J. Propulsion. Power. **10**(5), 676–682 (1994). <https://doi.org/10.2514/3.23779>
  30. Eppler, R., Hepperle, M.: "A Procedure for Propeller Design by Inverse Methods", in Proceedings of the International Conference on Inverse Design Concepts in Engineering Sciences (ICIDES), Dulikravich, G. S., Ed., Austin, TX, (17.-18. October 1984), pp. 445–460
  31. Hepperle, M.: "Inverse Design Procedure for Propellers Having a Prescribed Chord-Length Distribution," Journal of Aircraft, vol. 47, no. 6, pp. 1867–1872, (November-December, 2010)
  32. Hepperle, M.: Javaprop Users Guide, Available online at <https://www.mh-aerotools.de/airfoils/javaprop.htm>, (Retrieved August 2020)
  33. Hashin, Z.: Failure Criteria for Unidirectional Fiber Composites. Journal of Applied Mechanics **47**, 329–334 (1980). <https://doi.org/10.1115/1.3153664>
  34. Wiedemann, J.: Leichtbau: Elemente und Konstruktion (in English: Lightweight Construction: Elements and Construction) (Klassiker der Technik). Springer Berlin Heidelberg, (2007), isbn:9783540336570
  35. Voß, A., Handojo, V., Weiser, C., Niemann, S.: "Preparation of Loads and Aeroelastic Analyses of a High Altitude, Long Endurance, Solar Electric Aircraft," AEC2020 Aerospace Europe Conference, (2020)
  36. Rodden, W., MacNeal, Harder, R., McLean, Bellinger, D.: MSC. Nastran Version 68 Aeroelastic Analysis User's Guide. MSC Software Corporation, (2010)
  37. Rodden, W.P.: Theoretical and computational aeroelasticity. Crest Pub, Burbank, California (2011)
  38. Voß, A.: "Design and Structural Optimization of a Flying Wing of Low Aspect Ratio Based on Flight Loads," DLR Institute of Aeroelasticity, Göttingen, Germany, Research Report DLR-FB-2020-20, (March 2020), Available online at <https://elib.dlr.de/134626/>
  39. Raab, C.: "Aerodynamikmodell für das Forschungsflugzeug A320 ATRA (in English: Aerodynamic Model for the Research Aircraft A320 ATRA)," DLR Institute of Flight Systems, Tech. Rep. DLR-IB 111-2010/45, (2010)
  40. Federal Aviation Administration, "Airplane Simulator Qualification," FAA Advisory Circular, Tech. Rep., (July 1995)
  41. Jategaonkar, R. V.: Flight Vehicle System Identification - A Time Domain Methodology: Second Edition (Progress in Astronautics and Aeronautics). Reston, VA, USA: AIAA, (2015), vol. 245, ISBN: 978-1-62410-278-3
  42. Mönnich, W.: "Ein 2-Punkt-Aerodynamikmodell für die Identifizierung (in English: A 2-Point Aerodynamic Model for the Identification)," in Symposium "Systemidentifizierung in der Fahrzeugdynamik". DFVLR Mitteilung 87-22, Paper No. 3.1, (1987)
  43. Fischenberg, D.: "Identification of an unsteady aerodynamic stall model from flight test data," in Proceedings of the AIAA 1995 Atmospheric Flight Mechanics Conference, AIAA-95-3438-CP, Baltimore, MD, USA, (September 1995). <https://doi.org/10.2514/6.1995-3438>
  44. Fischenberg, D.: "Identifizierung des Bodeneffektes und der Fahrwerksaerodynamik des ATTAS aus Flugversuchsdaten (in English: Identification of the Ground Effect and the Landing Gear Aerodynamics of the ATTAS Based on Flight Test Data)," DLR Institute of Flight Mechanics, Tech.Rep. DLR-IB 111-94/22, (1994)
  45. Voß, A., Handojo, V., Weiser, C., Niemann, S.: "Results from Loads and Aeroelastic Analyses of a High Altitude, Long Endurance, Solar Electric Aircraft," in Journal of Aeroelasticity and Structural Dynamics, vol. 9, Department of Aerospace Engineering of Politecnico di Milano, (January 2022). <https://doi.org/10.3293/asdj.2021.58>
  46. Waszak, M.R., Schmidt, D.K.: Flight dynamics of aeroelastic vehicles. J. Aircraft. **25**, 563–571 (1988). <https://doi.org/10.2514/3.45623>
  47. Schmidt, D.: Modern flight dynamics. McGraw-Hill Education, (2011), isbn: 9780073398112
  48. Weiser, C., Ossmann, D.: "Baseline flight control system for high altitude long endurance aircraft," in AIAA SCITECH 2022 Forum. American Institute of Aeronautics and Astronautics (2022). <https://doi.org/10.2514/6.2022-1390>
  49. SAE International, AS94900 Vehicle Management Systems-General Specification Guide for Flight Control Function, Design, Installation and Test of Piloted Military Aircraft, Available online at <https://www.sae.org/standards/content/as94900a>, (2018)
  50. Stevens, B., Lewis, F., Johnson, E.: Aircraft Control and Simulation: Dynamics, Controls Design, and Autonomous Systems, 3rd Edition. Wiley, (2015), isbn: 9781118870983
  51. Ossmann, D., Luspay, T., Vanek, B.: "Baseline Flight Control System Design for an Unmanned Flutter Demonstrator," 2019 IEEE Aerospace Conference, pp. 1–10, (March 2019), issn: 1095-323X. <https://doi.org/10.1109/AERO.2019.8741853>
  52. Joos, H.-D., Bals, J., Looye, G., Schnepfer, K., Varga, A.: "A multi-objective optimisationbased software environment for control systems design," in IEEE International Conference on Control Applications and International Symposium on Computer Aided Control Systems Design, (September 2002), pp. 7–14
  53. Apkarian, P., Gahinet, P., Buhr, C.: "Multimodel, multi-objective tuning of fixed-structure controllers," 2014 European Control Conference (ECC), pp. 856–861, (2014)
  54. Apkarian, P., Dao, M., Noll, D.: Parametric Robust Structured Control Design. IEEE Transactions on Automatic Control **60**, 1857–1869 (2015). <https://doi.org/10.1109/TAC.2015.2396644>

55. Müller, R., Kiam, J.J., Mothes, F.: "Multiphysical simulation of a semi-autonomous solar powered high altitude pseudo-satellite," in. IEEE Aerospace Conference **2018**, 1–16 (2018). <https://doi.org/10.1109/AERO.2018.8396531>
56. European Aviation Safety Agency, Certification Specifications for Sailplanes and Powered Sailplanes-CS-22, Amendment 2, (2009)
57. Department of Defense, USA, Military Standard, Flying Qualities of Piloted Aircraft, MIL-STD-1797A, (July 2001)
58. European Aviation Safety Agency, Certification Specifications for Large Aeroplanes - CS-25, Amendment 3, (2007)
59. Diederich, F.: "Calculation of the effects of structural flexibility on lateral control of wings of arbitrary plan form and stiffness," Langley Aeronautical Laboratory, Langley Field, USA, NACA

Research Memorandum, (December 1948), Available online at <https://ntrs.nasa.gov/citations/19930085464>

**Publisher's Note** Springer Nature remains neutral with regard to jurisdictional claims in published maps and institutional affiliations.